Monthly Notices of the ROYAL ASTRONOMICAL SOCIETY

MNRAS **541,** 2440–2458 (2025) https://doi.org/10.1093/mnras/staf516
Advance Access publication 2025 April 1

E-INSPIRE – I. Bridging the gap with the local Universe: stellar population of a statistical sample of ultra-compact massive galaxies at $z < 0.3$

John Mills,[1] Chiara Spiniello ,[1,2★] Alexey Sergeyev,[3,4,5] Crescenzo Tortora ,[2] Vladyslav Khramtsov ,[6] Giuseppe D'Ago ,[7] Michalina Maksymowicz-Maciata,[8] João P. V. Benedetti ,[9,10] Anna Ferré-Mateu ,[9,10] Michele Cappellari ,[1] Roger Davies,[1] Johanna Hartke [11,12] and Charles Rosen[1]

[1]*Sub-Department of Astrophysics, Department of Physics, University of Oxford, Denys Wilkinson Building, Keble Road, Oxford OX1 3RH, UK*
[2]*INAF – Osservatorio Astronomico di Capodimonte, Via Moiariello 16, I-80131 Naples, Italy*
[3]*Observatoire de la Côte d'Azur, Université Côte d'Azur, CNRS, Laboratoire Lagrange, CS 34229, 06304 Nice Cedex 4, France*
[4]*Research Institute of Astronomy,V. N. Karazin Kharkiv National University, 61022, Sumska 35, Kharkiv, Ukraine*
[5]*Institute of Radio Astronomy of National Academy of Science of Ukraine, 61002, Mystetstv 4, Kharkiv, Ukraine*
[6]*Department of Astronomy and Space Informatics, V. N. Karazin Kharkiv National University, 35 Sumska Str, 61022, Kharkiv, Ukraine,*
[7]*Institute of Astronomy, University of Cambridge, Madingley Road, Cambridge CB3 0HA, UK*
[8]*Astrophysics Group, H. H. Wills Physics Laboratory, University of Bristol, Tyndall Avenue, Bristol BS1 8TL, UK*
[9]*Instituto de Astrofísica de Canarias, Vía Láctea s/n, E-38205 La Laguna, Tenerife, Spain*
[10]*Departamento de Astrofísica, Universidad de La Laguna, E-38200 La Laguna, Tenerife, Spain*
[11]*Finnish Centre for Astronomy with ESO (FINCA), University of Turku, FI-20014 Turku, Finland*
[12]*Tuorla Observatory, Department of Physics and Astronomy, University of Turku, FI-20014 Turku, Finland*

Accepted 2025 March 26. Received 2025 March 26; in original form 2024 October 21

ABSTRACT

This paper presents the first effort to Extend the Investigation of Stellar Populations In RElics (E-INSPIRE). We present a catalogue of 430 spectroscopically confirmed ultra-compact massive galaxies (UCMGs) from the Sloan Digital Sky Survey at redshifts $0.01 < z < 0.3$. This increases the original INSPIRE sample eightfold, bridging the gap with the local Universe. For each object, we compute integrated stellar velocity dispersion, age, metallicity, and [Mg/Fe] through spectroscopic stellar population analysis. We infer star formation histories (SFHs), metallicity evolution histories (MEHs) and compute the *Degree of Relicness* (DoR) of each object. The UCMGs, covering a wide range of DoR from 0.05 to 0.88, can be divided into three groups, according to how extreme their SFH was. The first group consists of 81 extreme relics (DoR $\gtrsim 0.6$) that have formed the totality of their stellar mass by $z \sim 2$ and have super-solar metallicities at all cosmic epochs. The second group ($0.3 \lesssim$ DoR $\lesssim 0.6$) contains 293 objects also characterized by peaked SFHs but with a small percentage of later-formed stars and with a variety of MEHs. The third group (DoR $\lesssim 0.3$), has 56 objects that cannot be considered relics since they have extended SFHs and formed a non-negligible fraction (>25 per cent) of their stellar mass at $z < 2$. We conclude that the most efficient method of finding relics is to select UCMGs with a combination of large velocity dispersion values (as already found by INSPIRE), super-solar metallicities and high [Mg/Fe].

Key words: galaxies: elliptical and lenticular, cD – galaxies: evolution – galaxies: formation – galaxies: kinematics and dynamics – galaxies: star formation – galaxies: stellar content.

1 INTRODUCTION

Relics (Trujillo et al. 2009), the nearby counterpart of high-z 'red-nuggets' (Damjanov et al. 2009), are the perfect local laboratories to investigate the early phases of the mass assembly and formation scenarios of massive galaxies. In fact, they are almost exclusively composed of 'pristine', very old stellar populations that formed at very high-z and evolved passively and undisturbed thereafter.

Relics are, however, very rare: their local density at $z < 0.5$ ranges between 10^{-7} and 10^{-5} Mpc^{-3} and declines at low redshift (Charbonnier et al. 2017; Ferré-Mateu et al. 2017; Tortora et al. 2018; Spiniello et al. 2021b). This is the reason why the INvestigating Stellar Population In RElics (INSPIRE) Project started a systematic effort to build a statistically large sample of relics (Spiniello et al. 2021a, b, 2024; D'Ago et al. 2023; Martín-Navarro et al. 2023; Maksymowicz-Maciata et al. 2024). Thanks to an ESO Observational Large Programme, the INSPIRE survey has targeted, with the X-Shooter spectrograph (XSH; Vernet et al. 2011), 52 spectroscopically confirmed red ultra-compact massive galaxies (UCMGs). These

★ E-mail: chiara.spiniello@physics.ox.ac.uk

objects are defined as outliers on the stellar-mass size relation for early-type galaxies (ETGs; e.g. Shen et al. 2003), being 4–5 times more compact than normal-sized galaxies with similar stellar mass. Many mass and size thresholds have been used in the literature to define UCMGs (Charbonnier et al. 2017). In particular, the 52 INSPIRE targets have been selected to have optical median effective radii $R_e < 2$ kpc, stellar masses $M_\star > 6 \times 10^{10}\,M_\odot$, redshifts $0.1 < z < 0.4$, and red colours (see fig. 1 in Spiniello et al. 2021b). Among these, 38 had formed 75 per cent or more of their stellar mass at $z > 2$, and were thus classified as relics (Spiniello et al. 2024). In terms of structural parameters and photometry, both relics and non-relics in INSPIRE are red, but span a large range of Sérsic indices (n), and axial ratios (q). These quantities were obtained in Tortora et al. (2016, 2018) and Scognamiglio et al. (2020) by fitting a point-spread function (PSF) convolved Sérsic profile to g, r, i images from the Kilo Degree Survey (KiDS; Kuijken 2011), using the code 2DPHOT (La Barbera et al. 2008).

For each of the UCMGs, Spiniello et al. (2024)[1] computed a *Degree of Relicness* (DoR; Ferré-Mateu et al. 2017). The DoR is a dimensionless number obtained as the mean of three quantities: the fraction of stellar mass formed by $z = 2$, the inverse of the cosmic time at which a galaxy has assembled 75 per cent of its mass, and the inverse of the final assembly time renormalized by the redshifts of the objects (see equation 1 in INSPIRE DR3). Hence, practically, a higher DoR corresponds to a very early and quick mass assembly: the most extreme relics that have assembled the totality of its stellar mass only 0.7 Gyr after the big bang would have DoR = 1, while an object with a very extended star formation history (SFH) that is still forming a small percentage of stars would have DoR = 0. For reference, by this definition NGC 1277, the bonafide massive relic in the local Universe, has a DoR of ∼0.95.

Characterizing the first large sample of relics, INSPIRE has provided hints on how to search for these rare objects. Hence, now, with the Extension of the INvestigating Stellar Populations In RElics (E-INSPIRE) project, we aim at extending in redshift, stellar mass and wavelength the current sample of UCMGs with a measured DoR, with the goal of collecting a statistically large sample of ultra-compact galaxies, looking for the most extreme relics in our Universe. Since relics are the 'building blocks' of today's giant ETGs, the E-INSPIRE project will allow us to shed light on the formation and evolution of this population of galaxies that account for more than half of the total stellar mass in the Universe and are responsible for most of its chemical enrichment.

In this paper, the first of the new series, we start by extending the redshift coverage of INSPIRE by searching for relics in the redshift window $0.01 < z < 0.3$, hence bridging the gap with the very few known relics in the local Universe (Trujillo et al. 2014; Ferré-Mateu et al. 2017; Yıldırım et al. 2017).

One of the main results obtained so far from INSPIRE is that the DoR strongly correlates with the integrated stellar velocity dispersion ($\sigma_\star$). Relics (UCMGs with higher DoR) have larger $\sigma_\star$ than non-relic UCMGs and normal-sized ETGs of similar stellar mass (Spiniello et al. 2021b; Maksymowicz-Maciata et al. 2024). Hence, selecting compact galaxies with a very high-velocity dispersion seems to be a very effective way to select relic candidates. There have been previous efforts to search for compact galaxies with higher stellar velocity dispersions at low redshifts within the Sloan Digital Sky Survey (SDSS), such as Saulder, van den Bosch & Mieske (2015) and Clerici et al. (2024). SDSS is ideal to search for these very rare systems due to the wide sky coverage of more than 8000 square degrees. Very recently, Clerici et al. (2024) presented a stellar population study of 1858 compact massive galaxies selected to be outliers in the $\log\sigma_\star$–$\log R_e$ and in the $\log M_\star$–$\log\sigma_\star$ planes. However, their sample was limited to $\sigma_\star < 380\,\mathrm{km\,s^{-1}}$ due to the belief that values above this were not to be trusted. While this may be true in some cases, previous results have demonstrated that both nearby relics (Trujillo et al. 2014; Ferré-Mateu et al. 2017; Spiniello et al. 2024) and high-z red nuggets (Saracco et al. 2020) can have velocity dispersions even higher than this value. Furthermore, an incredibly high value measured for the integrated velocity dispersion could also be due to a combination of an unresolved rotation added on top of a large velocity dispersion with a rather flat spatial profile. Hence, we believe that the most effective approach to search for relics requires searching through the full range of $\sigma_\star$, and then manually checking the full spectral fitting to assess its quality. This is what we proceeded to do in this paper.

The paper is organized as follows. In Section 2, we introduce the sample, highlighting the selection criteria used to define UCMGs. In Section 3, we present the spectral analysis, including the computation of the signal-to-noise ratio (SNR), the integrated stellar velocity dispersion ($\sigma_\star$), and the stellar population parameters. In particular, we infer the SSP-equivalent [Mg/Fe] ratios with line-indices and age and metallicity via full-spectral fitting. Section 4 presents our main findings: SFH and metallicity evolution, as well as the calculation of the DoR for each of the objects and the subsequent confirmation of 435 new relics at $z \leq 0.3$. We finally conclude in Section 5.

Throughout the paper, we assume a standard Lambda cold dark matter cosmology with $H_0 = 67.7\,\mathrm{km\,s^{-1}\,Mpc^{-1}}$, $\Omega_\Lambda = 0.689$, and $\Omega_M = 0.311$ (Planck Collaboration VI 2020).

2 DATA SELECTION

This section outlines the steps we undertake to identify compact galaxies and select UCMGs from optical SDSS images and associated, publicly available photometric catalogues.

2.1 Initial selection of objects

We use spectroscopic data from the SDSS DR18 (Almeida et al. 2023) to select extra-galactic, bright, and red objects with high stellar velocity dispersion values. In particular, we run a SQL search retrieving objects from the imaging (PhotoObj) and spectroscopic (SpecObj) SDSS catalogues with the following criteria:

(i) redshift $0.005 < z < 0.4$. The lower limit ensures the removal of galactic contaminants (stars), while the upper limit is set to have the same stellar absorption lines available for INSPIRE objects;
(ii) Petrosian magnitude in the $r-$band $\mathrm{mag}_r < 20$, which roughly corresponds to the same magnitude cut of INSPIRE objects and makes the recovery of structural parameters trustable;
(iii) colour $g - i > 1.2$, to select systems with an evolved stellar populations;
(iv) stellar velocity dispersion $\sigma_\star > 200\,\mathrm{km\,s^{-1}}$, which is the typical values for normal-sized galaxies with $M_\star \geq 10^{10}\,M_\odot$. However, we exclude objects with $\sigma_\star = 850\,\mathrm{km\,s^{-1}}$ exactly (the maximum value given in the catalogues) because this is likely more indicative of a bad fit rather than an object with a very high $\sigma_\star$.

Furthermore, we only keep systems with no 'zWarning' and exclude those with the keyword 'class' set to 'STARBURST', 'STARFORMING', 'STARFORMING BROADLINE', or 'STARBURST BROADLINE'. As stated in Bolton et al. (2012), these

[1]The 5th paper of the series which also presented the third ESO data release.

classes are defined as systems with emission lines in H β, [O III] 5007, H α, and [N II] 6583 detected at the 3 σ level which also satisfy $\log_{10}([\mathrm{O\,III}]/\mathrm{H}\,\beta) < 1.2\ \log_{10}([\mathrm{N\,II}]/\mathrm{H}\,\alpha) + 0.22$. Systems are further designated 'STARFORMING' if the equivalent width of the H α line is less than 50 Å and 'STARBURST' if it is greater than 50 Å. A system is set as 'BROADLINE' if the line widths are greater than 200 km s^{-1} with line-width measurement at the 5σ level and line-flux measurement at the 10σ level. Since relics, by definition, have formed most of their stellar mass by $z = 2$, they should have low star-formation rates. The described SQL search produces an initial shortlist of 387 949 objects.

To find objects that are UCMGs, we need to obtain an estimate of their stellar masses ($M_\star$). We therefore cross-match our shortlist with the GALEX–SDSS–WISE Legacy Catalogue[2], specifically GSWLC-2 (Salim, Boquien & Lee 2018). The catalogue contains stellar masses, dust attenuation and star formation rates of ∼700 000 galaxies with SDSS redshifts below 0.3 and magnitudes $\mathrm{mag}_r < 18$. The galaxy properties are obtained via spectral energy distribution (SED) fitting using a Bayesian framework on joint UV + optical + mid-IR data. From these quantities, we also calculate the specific star formation rate (sSFR) for each object, simply dividing the star formation rate by the stellar mass. Cross-matching the GSWLC-2 catalogue with our initial shortlist returns 126 898 objects, where we exclude any objects with 'flag_sed' $\neq 0$ which indicates a poor fit. We also note that this cross-match introduces an additional cut in both redshift and $r-$band magnitude, since GSWLC-2 only covers $0.01 < z < 0.3$ and $\mathrm{mag}_r < 18.0$.

2.2 Selection of compact galaxies using compactness

SDSS provides several proxies for the effective radii (R_e) of the galaxies. In particular, we consider the estimates from the de Vaucouleurs (deVRad) and exponential (expRad) fits, along with the radii containing 50 per cent of the Petrosian flux (petroR50). The Petrosian flux is defined in SDSS as the total flux within two times the Petrosian radius, where the Petrosian radius (petroRad) is the radius at which the ratio of the local surface brightness in an annulus to the mean surface brightness within the same radius reaches the value of 0.2 (Blanton et al. 2001; Yasuda et al. 2001; Stoughton et al. 2002). Even though the Petrosian radius is the least dependent on redshift,[3] we cannot select UCMGs directly on the basis of this quantity since it does not take into account the PSF. This has a noticeable effect for objects with $R_\mathrm{e} < 2$ arcsec (Blanton et al. 2001), which includes many of our objects of interest.

SDSS also provides a coefficient ranging between 0 and 1 called FRACDEV (f_deV) which describes the relative contribution to the total luminosity of the de Vaucouleurs fit with respect to the exponential one (Abazajian et al. 2004).

To estimate the sizes of each object, we follow the approximation of Baldry et al. (2021) and use the geometric mean of the two models, weighted by the f_deV coefficient:[4]

$$\log R_\mathrm{e} = f_\mathrm{deV} \log R_\mathrm{deV} + (1 - f_\mathrm{deV}) \log R_\mathrm{exp}. \quad (1)$$

[2]GALEX and WISE refer to the Galaxy Evolution Explorer and the Wide-field Infrared Survey Explorer respectively.

[3]According to Blanton et al. (2001) the flux contained in the Petrosian half-light radius is completely independent of redshift except when the size of the galaxy is comparable to the seeing, which is the case for our data.

[4]This measure of R_e compares well with the Simard et al. (2011) catalogue (Baldry et al. 2021), especially when using the geometric mean as opposed to the linear weighted mean.

Finally, we convert the effective radius of every object from arcsec to kpc with the ASTROPY.COSMO PYTHON package (Astropy Collaboration 2022),[5] where we use the redshifts obtained from SDSS.

There are many criteria by which one can select UCMGs. The most commonly used in the literature are those setting two separate thresholds on the stellar mass and the size (see e.g. Charbonnier et al. 2017 for a list of commonly used definitions). Previously in INSPIRE, we have followed this approach and defined a UCMG as an object with $R_\mathrm{e} < 2$ kpc and $M_\star > 6 \times 10^{10}\,\mathrm{M}_\odot$ (Spiniello et al. 2021b). The main limitation of this criterion, however, is that it neglects the size–mass distribution of galaxies, plotted in the top panel of Fig. 1. This means that one automatically excludes the most massive objects, which are relatively bigger by definition but still clear outliers with respect to the main population. Here, following Barro et al. (2013), we define the quantity $\Sigma_{1.5} = M_\star / {R_\mathrm{e}}^{1.5}$ which measures the compactness of the objects. This choice of exponent is roughly consistent with what is found by Newman et al. (2012) for quiescent galaxies and also traces the size–mass distribution observed in Fig. 1. Compact galaxies are then defined as outliers in the the size–mass distribution, using the same threshold defined in Baldry et al. (2021): $\log \Sigma_{1.5} > 10.5$.

In the bottom panel of Fig. 1, we plot the effective radii against the velocity dispersion values as computed by SDSS. Compact galaxies follow a similar distribution as that of the general population of galaxies from the GSWLC-2 catalogue, the only difference being that they have smaller R_e (by definition).

From the galaxies in our input sample, 628 pass the compactness threshold. However, we note that among these, a number of contaminants are expected (e.g. Khramtsov et al. 2019). First of all, the classification could be wrong for some of the objects, which can be quasars. Or, more commonly, a larger galaxy with a bright stellar nucleus could have a small measured half-right radius as this is set by the nucleus alone. Hence, we visually inspected the stamps and SDSS spectra for all the retrieved objects, finally selecting 495 compact galaxies, for which we retrieved the 1D spectra directly from SDSS. Histograms characterizing the overall properties of the UCMGs can be found in Fig. 2.

2.3 Selection of UCMGs

The left-most histogram of Fig. 2 shows the effective radii of the 495 compact galaxies. Although the peak of the distribution is at $R_\mathrm{e} < 2$ kpc, an extended tail is visible at larger sizes. This is because, differently from what has been done previously, we do not impose any upper limit on the effective radii during the selection. Hence, this novel approach could, in principle, make it slightly more complicated to perform a direct comparison between this work and previous INSPIRE selections. However, we note that the effective radii measured from KiDS data (in Tortora et al. 2018 and Scognamiglio et al. 2020), fitting a PSF convolved Sérsic profile to the images using the code 2DPHOT (La Barbera et al. 2008), are systematically smaller than the ones inferred from SDSS imaging. We believe this is because SDSS has a worse spatial resolution and a larger pixel size, as shown in Fig. B1 of Appendix B. There, we compute a correction factor based on the 36 objects that appear in both SDSS and INSPIRE. When correcting the SDSS-based effective radii, 446 out of the 495 galaxies selected with the compactness criterion have $R_{\mathrm{e\,KiDS}} \leq 2$ kpc (corresponding to a $R_{\mathrm{e\,SDSS}} \lesssim 4$ kpc, see Fig. B2)

[5]https://www.astropy.org

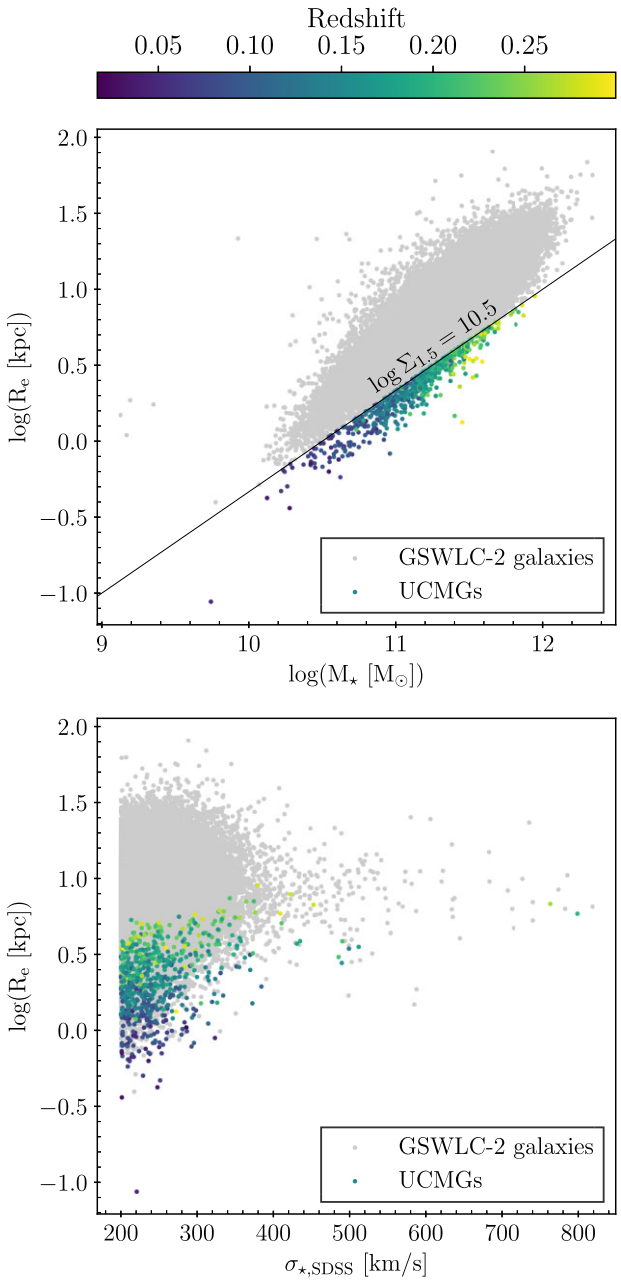

Figure 1. The relations between size and stellar mass (top) and size and velocity dispersion (bottom) for objects in our sample (coloured points) and the entire GSWLC-2 catalogue (grey points). We have selected as UCMGs the objects that satisfy $\log \Sigma_{1.5} = \log(M_\star / R_e{}^{1.5}) > 10.5$. The UCMGs are colour-coded by redshift. We observe a positive correlation between redshift and stellar mass (and therefore effective radius) because we are only concerned with objects with $\mathrm{mag}_r < 18$, which systematically filters out less massive objects which are further away.

and hence can be considered ultra-compact. We further note that our SDSS sample covers a wider range in stellar mass than INSPIRE, also including a small number of less-massive objects. Hence, we further remove from the sample galaxies with $M_\star \leq 6 \times 10^{10}\,\mathrm{M}_\odot$.

In the remainder of the paper, we will limit ourselves to the remaining 430 objects which can be considered ultra-compact massive galaxies (UCMGs, blue histograms in Fig. 2) and hence compared with the INSPIRE higher-z counterparts.

3 DATA ANALYSIS

3.1 Stellar kinematics

Although SDSS has already computed and published the stellar velocity dispersion values for all these systems, we re-derive them using the PENALISED PIXEL-FITTING software[6] (PPXF; Cappellari & Emsellem 2004; Cappellari 2017, 2023). As stellar library for the fit, we employ the E-MILES Single Stellar Population (SSP) models (Vazdekis et al. 2016), which are distributed together with the PPXF code.

For each system, we derive two values of the velocity dispersion, one using the restricted (rest frame) wavelength range (3600–6500)Å ($\sigma^{\mathrm{res}}_{\star,\mathrm{ppxf}}$) for all galaxies, and one using the full wavelength range of the spectra ($\sigma^{\mathrm{full}}_{\star,\mathrm{ppxf}}$). For this latter value the covered wavelength of SDSS (3800–9200 Å) slightly changes from galaxy to galaxy, according to their redshift.

We compute $\sigma^{\mathrm{res}}_{\star,\mathrm{ppxf}}$ to be consistent with deriving the stellar population parameters in Section 3.3.2 and to use only the cleanest spectra region. We compute $\sigma^{\mathrm{full}}_{\star,\mathrm{ppxf}}$ instead to maximise the data used to calculate the velocity dispersion and to compare the results we obtain with those published by the SDSS survey. We also note that, given the different redshifts of the objects, the $\sigma^{\mathrm{full}}_{\star,\mathrm{ppxf}}$ is computed on a slightly different wavelength range for each galaxy. In both cases, we set the additive Legendre polynomial degree (DEGREE) to 20 and use the keyword CLEAN to perform sigma-clipping on the spectra and clean them from residual bad pixels. We refer the reader to INSPIRE DR2 for extensive testing on how the inferred velocity dispersion values change when changing the parameters of the fit (stellar templates, wavelength range, additive polynomial, masked regions, etc.). In the same paper, we also demonstrated that the systematic uncertainties associated with the velocity dispersion depend on the SNR of the spectrum (see fig. 6 in INSPIRE DR2) and dominate the error budget. Hence, following the same approach, although the random errors given by the code are always of the order of 1 per cent, we attribute a final total (systematic and random) uncertainty of 5 per cent to the objects with a spectrum with SNR > 30, and an uncertainty of 10 per cent for galaxies with spectra of lower SNR. We note that the uncertainties from SDSS only include random errors.

Overall, a good agreement is found between the velocity dispersion values from SDSS and these inferred by us, as shown in the upper panel of Fig. 3. The solid line shows the line of best fit, calculated with the LTSFIT PYTHON package,[7] which implements the method described in Section 3.2 of Cappellari et al. (2013) and uses the Least Trimmed Squares (Rousseeuw & Van Driessen 2006) technique to iteratively clip outliers. The fit is very similar to the 1-to-1 relation (in red), especially for $\sigma_\star$ up to $\sim$500 km s^{-1}. The sigma estimated from PPXF differs by more than 2.6σ (containing 99 per cent of systems if the residuals followed a perfectly Gaussian distribution, dotted lines) only for 10 systems. This means that we would expects roughly five spurious outliers out of 500 measures, similar to what we find. It should be noted that all but one of these objects have an SNR between $\sim$14 and $\sim$24, which is not particularly high when compared with the overall distribution in Fig. 4. The other object has SNR = 43.3.

We also observe excellent agreement between the two values of $\sigma_{\star,\mathrm{ppxf}}$ for the vast majority of systems, as shown in the lower panel of

[6] https://pypi.org/project/ppxf/
[7] https://pypi.org/project/ltsfit/

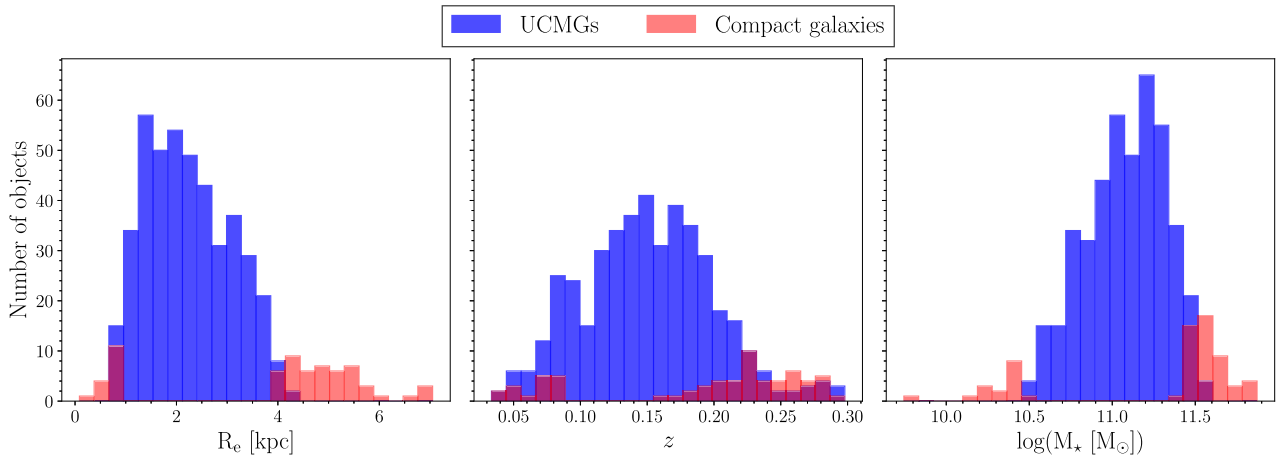

Figure 2. Histograms of the effective radii, redshifts, and stellar masses of the 495 compact galaxies. Out of these, 430 can be considered ultra-compact and massive according to the INSPIRE thresholds and are shown in blue. The other compact galaxies (either larger or less massive, as described in Section 2.3) are shown in red and have been excluded from the analysis. Note that the splitting between UCMGs and the rest is not a single threshold in size, but it is obtained using the equation (B1) to correct SDSS sizes to the KiDS resolution and then cutting everything with $R_{\rm e,KiDS} \leq 2$ kpc.

Fig. 3. Similarly to the upper panel, the best-fitting line is computed by the LTSFIT PYTHON package and is shown as a solid black line. This fit agrees very well with the 1-to-1 relation (in red) throughout the entire range of $\sigma_\star$. Only 10 out of 430 systems are not within 2.6σ of the best fit, however all but three have a SNR between ∼16 and ∼22, which is not particularly high (see Fig. 4). The other three systems have SNRs of 30.6, 30.7, and 43.3.

Since all three values of velocity dispersion that we have discussed agree very well with each other, we are free to only consider one of them for the rest of the analysis. Henceforth, we shall be referring to $\sigma^{\rm full}_{\star,\rm ppxf}$ when referring to velocity dispersion. A histogram of $\sigma^{\rm full}_{\star,\rm ppxf}$ for the UCMGs can be found in the bottom panel of Fig. 4.

Three examples of the systems with the highest, median, and lowest SNR are shown in Fig. 5, along with the system with the most extreme velocity dispersion as calculated by PPXF, while the results of SNR and velocity dispersion for a representative sample of the systems are listed in Table 1. The kinematical results for all 430 galaxies are provided in the online master catalogue associated with this publication.[8]

3.2 Signal-to-noise

We use the PYTHON routine DER_SNR[9] to calculate the integrated signal-to-noise (SNR) of each spectrum. This code assumes that the noise is Gaussian and uncorrelated in wavelength bins spaced two pixels apart. We only compute the SNR in the wavelength range in which we fit the stellar population parameters, which is (3600–6500)Å (see Section 3.3.2). The SNR per dispersive element ranges from ∼10 to ∼56, as shown in the histogram in the upper panel of Fig. 4. Such SNRs, listed in Table 1, are enough to infer stellar population parameters (Costantin et al. 2019).

3.3 Stellar population analysis

As in Spiniello et al. (2021b; INSPIRE DR1) and Spiniello et al. (2024; INSPIRE DR3), the stellar population analysis is performed in two separate steps. We first carry out a line-index analysis to infer the SSP-equivalent [Mg/Fe] ratios and then use full spectral fitting to estimate mass-weighted (and light-weighted) stellar ages and metallicities. This is mainly motivated by the fact that inferring [α/Fe] from full-spectral fitting and measuring the [Mg/Fe] from indices does not seem to be the same (Barbosa et al. 2021; Pernet, Boecker & Martín-Navarro 2024). Measuring [α/Fe] from full-fitting requires further tests (Vazdekis et al. 2015; Liu 2020) and hence we prefer to follow the steps already used in previous INSPIRE papers. This also ensures that the stellar population results and measurements for the two sets of galaxies can be directly compared.

During both steps, we use the same set of SSP models. Specifically, as already done for the kinematics (Section 3.1) and in previous papers, we use the MILES models (Vazdekis et al. 2015) with BaSTI theoretical isochrones[10] (Pietrinferni et al. 2004, 2006). From the MILES website,[11] we retrieve models with ages ranging from 0.5 to 14 Gyr in steps of 0.5 Gyr, and 10 different values of [M/H] ranging from −1.49 to +0.40 dex, and with the two publicly available values for the [α/Fe] abundance: 0.0 (solar) and 0.4 (super-solar).

The biggest assumption we make here concerns the Initial Mass Function (IMF), which we fix to a bimodal power law with a low-mass end logarithmic slope of 1.3, reproducing what has been done in INSPIRE DR3. This is broadly equivalent to a Salpeter IMF in terms of mass-to-light ratio estimates. We however point out that in Maksymowicz-Maciata et al. (2024) we have proven that relics prefer a bottom-heavier IMF than UCMGs with lower DoR. Unfortunately, however, to properly measure the IMF slope from each spectrum would require a higher SNR than is found in SDSS spectra. We cannot manually check each spectrum like in Maksymowicz-Maciata et al. (2024) due to the far greater number of objects and so we are forced to make the assumption of fixed IMF. In order to minimize the effect of this assumption on our results, we restrict the stellar population analysis to wavelengths bluer than 6500 Å, where the contribution to the light from M-dwarf stars is very small (Worthey 1994; Spiniello et al. 2014). The relic confirmation that we present in the results section is not affected by this assumption. However,

[8]The full catalogue is available on the E-INSPIRE webpage
[9]https://www.stecf.org/software/ASTROsoft/DER_SNR/

[10]http://www.oa-teramo.inaf.it/BASTI.
[11]http://research.iac.es/proyecto/miles/pages/webtools/tune-ssp-models.php

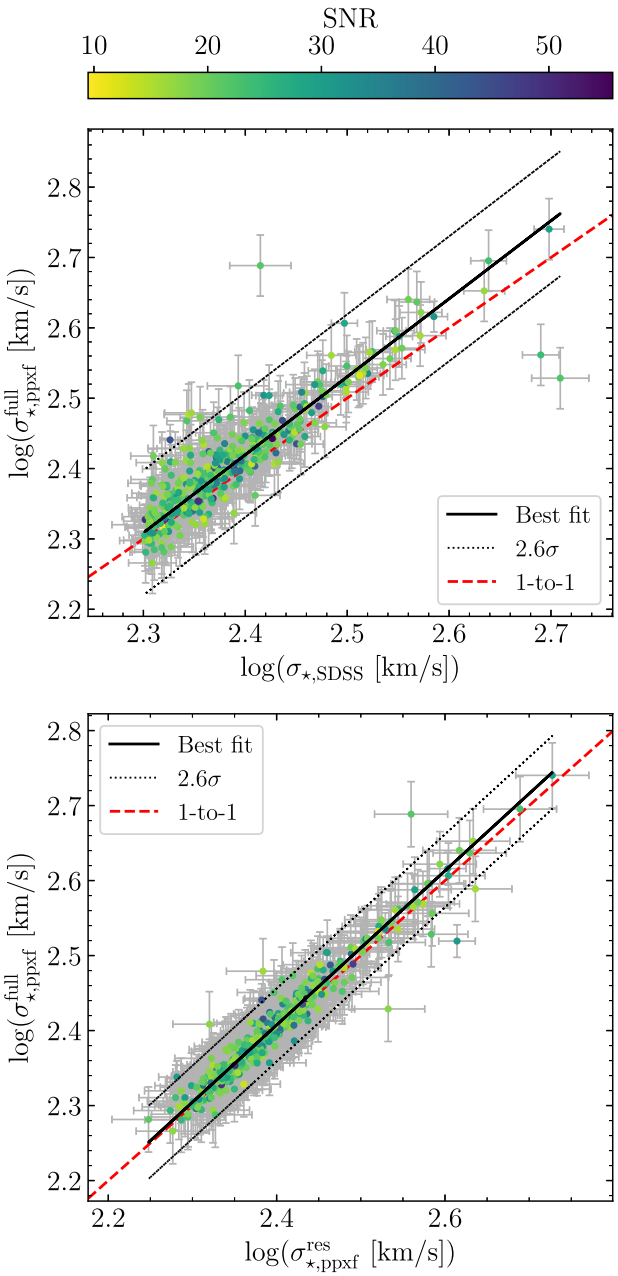

Figure 3. Top panel: comparison between the velocity dispersion values retrieved from SDSS (x-axis) and these computed here from the entire wavelength range covered by the spectra. A good agreement (within 2.6σ, dotted lines) is found for all but ten objects (see text for more details). Bottom panel: comparison between the velocity dispersion values computed using two different wavelength ranges. A good agreement is found for all but ten objects (see text for more details). For both panels, the best fit line is indicated by a solid black line and the 1-to-1 relation is indicated by a dashed red line. Additionally, the points are colour-coded by the SNR of the spectra.

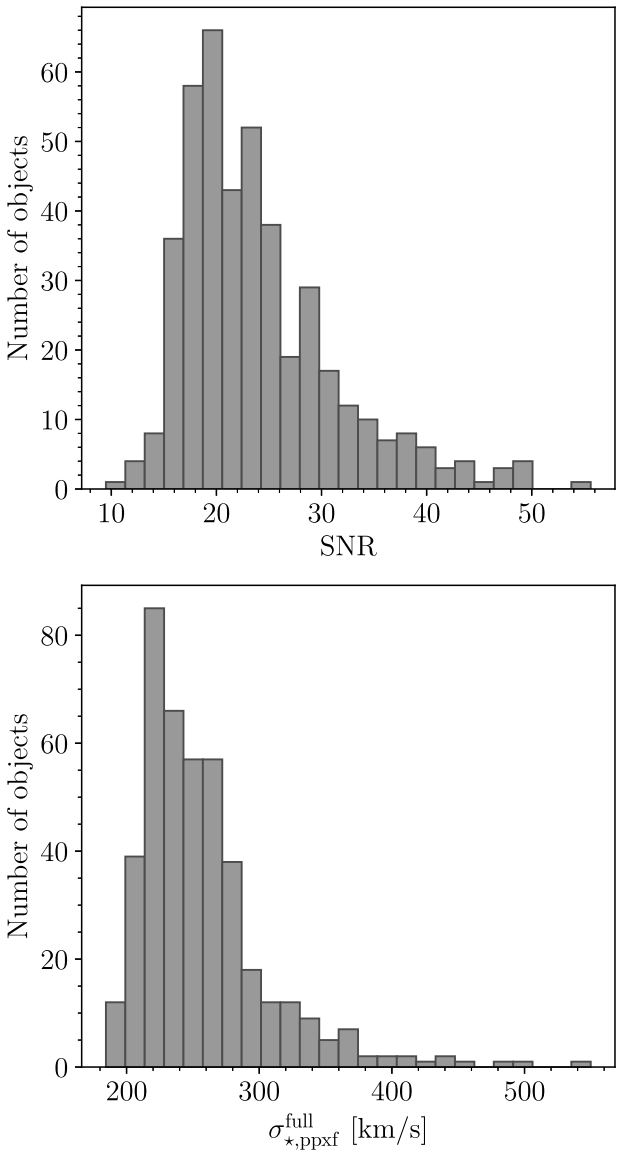

Figure 4. Top panel: histogram of the SNR per dispersive element for the UCMGs. Note that the SNR is calculated over the wavelength range (3600–6500)Å of each spectrum. Bottom panel: histogram of the velocity dispersions of the UCMGs, the calculation of which is discussed in Section 3.1.

we stress that by fixing the IMF, we bias our results by introducing a systematic offset to our derived values of [M/H] and ages, especially for low-DoR systems, (see appendix B in Maksymowicz-Maciata et al. 2024).

In future works, we will leverage the results achieved here and stack systems with similar SFHs to increase the resulting SNR and detect variation in the IMF slope at the population level.

3.3.1 SSP-equivalent [Mg/Fe] abundances from line-indices

The [Mg/Fe] abundance, computed from the stellar absorption lines, can be interpreted as the time-scale efficiency of the star formation episode. In fact, if the quenching occurs in a very short period, Type Ia supernovae do not have the time to pollute the interstellar medium with iron (e.g. Matteucci 1994; Thomas et al. 2005; Gallazzi et al. 2006, 2021) and hence the ratio is larger. Relics have indeed formed through a very fast star formation burst, and therefore they have a high, super-solar [Mg/Fe] ratio (Ferré-Mateu et al. 2017; Yıldırım et al. 2017; Martín-Navarro et al. 2018; Spiniello et al. 2021b, 2024).

We estimate the [Mg/Fe] via the analysis of line-index strengths from Mg and Fe lines. In particular, we take the $\rm Mg_b$ line (5177 Å) and the average of two different iron lines (Fe5270 and Fe5335), with the

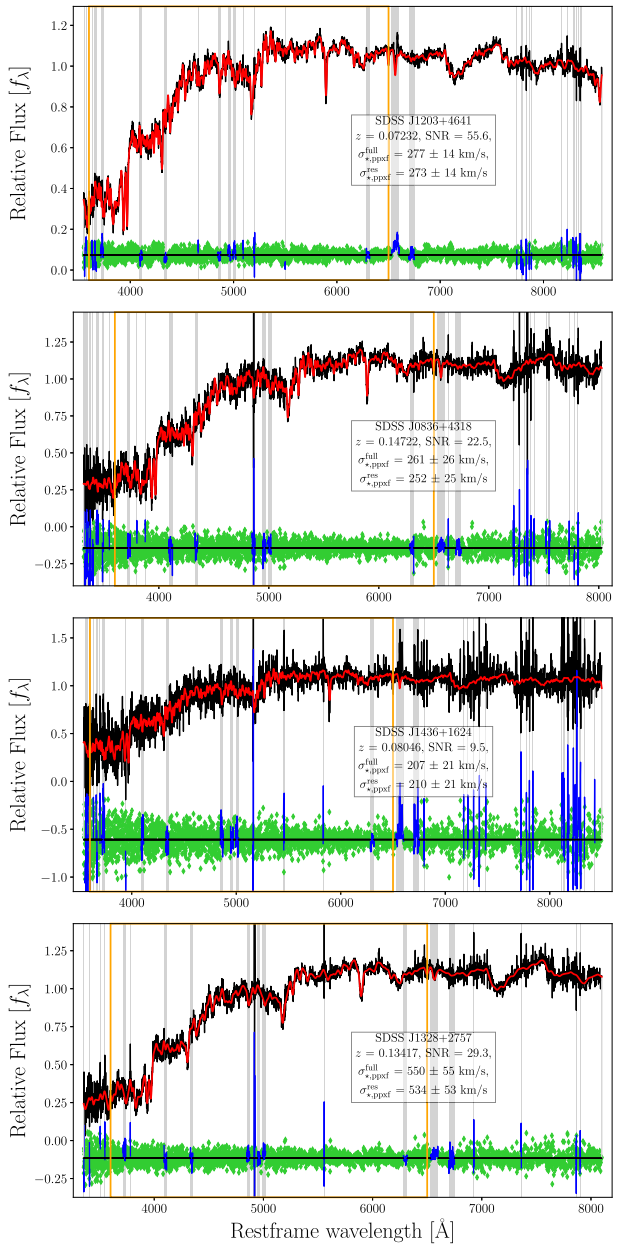

Figure 5. Examples of the PPXF kinematical fit for the (from top to bottom) best, middle, and worst SNR spectra, followed by the spectrum with the highest derived value of $\sigma_\star$. The galaxy is plotted in black while the best-fitting stellar template is overplotted in red. Green diamonds are the residuals and blue lines are points excluded by the fit (using the keyword CLEAN). The orange box indicates the wavelength range (3600–6500)Å, which is the restricted range where both the SNR and $\sigma^{\rm res}_{\star,\rm ppxf}$ are calculated. The inset in each panel lists the galaxy ID, the redshift, the integrated SNR and the two resulting velocity dispersions.

aim of minimizing the dependency on other elemental abundances (e.g. [Ti/Fe]) which might fall in the Fe-indices bandpasses.[12]

[12]We have however tested our results against the average of eight iron lines (Fe4383, Fe4531, Fe5015, Fe5270, Fe5335, Fe5406, Fe5709, Fe5782) and found that the inferred value of [α/Fe] does not change by more than our uncertainty of 0.1.

To calculate the strengths of these features from the galaxies' and the SSP's spectra, we use an in-house code (Benedetti et al. in preparation) which is a PYTHON implementation of the PACCE algorithm (Riffel & Borges Vale 2011). Unfortunately, the MILES models do not allow us to control [Mg/Fe] directly, but this can be approximated to [α/Fe], which is the parameter we can change in the SSPs. The version of the MILES models we employ here is only available at two different [α/Fe] abundances: 0.0 (solar) and 0.4. We therefore linearly interpolate the flux at each wavelength, building five sets of models with a Δ[α/Fe] = 0.1. We prefer not to extrapolate the models outside the original boundaries.

Differently from what we did in previous publications, here we do not convolve data and models to the same resolution. Instead, we account for variations in velocity dispersion and spectral resolution by computing 'correction factors' $C(\sigma)$, such that the corrected line-index strength is given by $I_{\rm corr} = I_{\rm orig} \times C(\sigma)$ (Davies, Sadler & Peletier 1993; Kuntschner 2004), where the I indicates the index under consideration. To compute these 'correction factors', we first download MILES models with resolutions covering the entire range of $\sigma_\star$, as derived in Section 3.1. Specifically, we use here models with a single value for metallicity ([M/H] = +0.06 dex), age (11 Gyr), and ([α/Fe]= 0.0). This is motivated by two pieces of evidence. First, we find that the 'correction factors' have minimal dependence on these stellar population parameters, especially for $\sigma_\star < 500\,{\rm km\,s^{-1}}$. Also, we note that in the Mg$_b$–$\langle$Fe$\rangle$ index–index plot, [α/Fe] (and hence [Mg/Fe]) varies in an orthogonal direction to [M/H] and age. Hence, this index–index plot makes us able to infer the [Mg/Fe], minimizing the uncertainties arising from changes in the other stellar population parameters. We then define $C(\sigma)$ for each model through $C(\sigma) = I(60\,{\rm km\,s^{-1}})/I(\sigma)$. To extend $C(\sigma)$ to all resolutions within the range $60 < \sigma_\star < 550\,{\rm km\,s^{-1}}$ (the upper limit is set by the highest velocity dispersion computed from PPXF in Section 3.1), we use a cubic spline interpolation, following the receipt outlined in Davies et al. (1993). We list these 'correction factors' in Table 2.

The overall effect of $C(\sigma)$ is that we can directly compare the UCMGs to SSP models with a resolution of $60\,{\rm km\,s^{-1}}$ (the minimum resolution of the MILES models to within our allowed uncertainty).

The results of the index calculation are shown in Fig. 6. The line-index strengths of the models with a resolution of $60\,{\rm km\,s^{-1}}$ are plotted, with models of equal metallicity joined by solid lines and models of equal [α/Fe] joined by dashed lines. The models with an age of 11 Gyr are in black whilst models with an age of 2 Gyr are shown in grey. We caution the reader that the models with [M/H] = 0.40 dex are outside the 'safe ranges'. However, we believe we can still use these models in the line-index analysis since [Mg/Fe] varies in an orthogonal direction to [M/H] (see the arrows on the top left corner), which means we can extrapolate beyond the 'safe ranges' in the direction of increasing metallicity without affecting the inference on the [Mg/Fe]. The UCMGs are plotted over the grids, where their line-index strengths have been corrected to a resolution of $60\,{\rm km\,s^{-1}}$. From the plot, we take as the 'true' value for [Mg/Fe] the [α/Fe] of the closest model to each point on the 11 Gyr grid. Given that there is no prior on age and metallicity and these will slightly shift the model grids, we assign an uncertainty of 0.1 to all the [Mg/Fe] values, which is equal to the steps between the models. These 'SSP-equivalent' [Mg/Fe] estimates will be used in the next section to select SSP models with a given [α/Fe] as input in the full-spectral fitting. There are a number of points falling outside the model grid. The majority of them (80) would be consistent with a larger [α/Fe], making them perfect relic candidates. A negative value of [α/Fe] (for 36 systems) could indicate instead a more extended SFH. However, we caution that these values might also be due to one

Table 1. Kinematic properties for a representative selection of SDSS UCMGs. For each system, we report the redshift, integrated optical SNR, the velocity dispersion value from SDSS, and those measured by PPXF, as described in Section 3.1. We also report the stellar mass and effective radii in both arcsec and kpc, the calculation of which is described in Section 2.3. The kinematic properties of all UCMGs in our sample is available in electronic form from the master catalogue.

ID SDSS	z	SNR per element	$\sigma_{\star,\mathrm{SDSS}}$ (km s^{-1})	$\sigma^{\mathrm{full}}_{\star,\mathrm{ppxf}}$ (km s^{-1})	$\sigma^{\mathrm{res}}_{\star,\mathrm{ppxf}}$ (km s^{-1})	$\log(M_\star\,[\mathrm{M}_\odot])$	R_e (arcsec)	R_e (kpc)
			Highest SNRs					
J1203+4641	0.0723	55.6	267 ± 6	277 ± 14	273 ± 14	11.26 ± 0.05	1.89 ± 0.01	2.69 ± 0.02
J2318+1507	0.1704	49.5	226 ± 6	226 ± 11	224 ± 11	11.47 ± 0.01	0.92 ± 0.01	2.77 ± 0.03
J1708+2723	0.1058	49.3	200 ± 5	213 ± 11	216 ± 11	11.07 ± 0.02	1.12 ± 0.01	2.25 ± 0.02
J1426+1647	0.0532	48.9	210 ± 4	212 ± 11	213 ± 11	10.70 ± 0.04	0.76 ± 0.01	0.82 ± 0.01
J1443+0739	0.0835	48.8	234 ± 5	228 ± 11	227 ± 11	11.18 ± 0.03	1.64 ± 0.02	2.66 ± 0.03
J1318+0114	0.0785	47.7	245 ± 5	252 ± 13	249 ± 12	10.89 ± 0.01	0.92 ± 0.01	1.41 ± 0.01
			Median SNRs					
J1512+4351	0.1300	22.5	209 ± 10	215 ± 21	210 ± 21	10.85 ± 0.04	0.54 ± 0.02	1.29 ± 0.04
J1540+1453	0.1134	22.4	234 ± 10	282 ± 28	249 ± 25	10.96 ± 0.01	0.80 ± 0.01	1.70 ± 0.02
J0040+0332	0.1667	22.4	272 ± 12	283 ± 28	301 ± 30	11.14 ± 0.03	0.86 ± 0.02	2.52 ± 0.05
J1350+2732	0.1400	22.4	229 ± 10	230 ± 23	238 ± 24	10.96 ± 0.03	0.68 ± 0.01	1.72 ± 0.03
J1138+3355	0.2379	22.4	230 ± 12	215 ± 21	219 ± 22	10.93 ± 0.05	0.48 ± 0.01	1.87 ± 0.05
J1550+5627	0.1792	22.2	297 ± 12	330 ± 33	319 ± 32	11.25 ± 0.01	0.80 ± 0.01	2.49 ± 0.04
			Lowest SNRs					
J1317+3640	0.1832	13.5	255 ± 16	255 ± 25	250 ± 25	11.31 ± 0.06	0.98 ± 0.03	3.13 ± 0.10
J0003+1607	0.1518	13.1	229 ± 15	213 ± 21	230 ± 23	11.00 ± 0.03	0.61 ± 0.01	1.68 ± 0.02
J1035−0045	0.1156	12.4	210 ± 14	218 ± 22	209 ± 21	10.76 ± 0.03	0.62 ± 0.01	1.33 ± 0.03
J0908+0656	0.2213	11.5	325 ± 18	341 ± 34	332 ± 33	11.45 ± 0.06	1.00 ± 0.04	3.69 ± 0.15
J1108+5006	0.1169	11.4	261 ± 16	262 ± 26	257 ± 26	10.90 ± 0.02	0.82 ± 0.02	1.79 ± 0.04
J1436+1624	0.0805	9.5	209 ± 18	207 ± 21	210 ± 21	10.69 ± 0.04	0.79 ± 0.01	1.23 ± 0.01
			Highest velocity dispersions from PPXF					
J1328+2757	0.1342	29.3	499 ± 17	550 ± 55	534 ± 53	11.46 ± 0.03	1.40 ± 0.02	3.45 ± 0.04
J0103+1426	0.1889	23.5	435 ± 18	496 ± 50	489 ± 49	11.48 ± 0.02	1.19 ± 0.02	3.86 ± 0.08
J2223−0012	0.2934	21.7	260 ± 18	488 ± 49	363 ± 36	11.55 ± 0.03	0.77 ± 0.03	3.50 ± 0.14
J1022+0521	0.1835	16.8	431 ± 20	449 ± 45	430 ± 43	11.39 ± 0.03	1.17 ± 0.03	3.72 ± 0.09
J0946+4929	0.1676	19.4	363 ± 18	437 ± 44	414 ± 41	11.26 ± 0.02	1.02 ± 0.03	3.01 ± 0.08
J1418+0807	0.1426	20.9	370 ± 15	433 ± 43	426 ± 43	11.23 ± 0.02	0.96 ± 0.03	2.50 ± 0.07
			Lowest velocity dispersions from PPXF					
J1126+0612	0.2702	18.9	212 ± 11	194 ± 19	197 ± 20	11.36 ± 0.02	0.78 ± 0.03	3.35 ± 0.12
J1704+2919	0.2079	22.2	208 ± 9	194 ± 19	212 ± 21	11.35 ± 0.04	0.99 ± 0.03	3.48 ± 0.11
J0956+6017	0.1142	23.0	205 ± 9	193 ± 19	197 ± 20	10.70 ± 0.01	0.57 ± 0.01	1.23 ± 0.02
J1346+2440	0.1675	21.1	209 ± 15	191 ± 19	177 ± 18	11.12 ± 0.03	0.87 ± 0.03	2.57 ± 0.09
J1303+3938	0.1198	24.9	201 ± 7	191 ± 19	194 ± 19	10.94 ± 0.01	0.85 ± 0.02	1.89 ± 0.04
J1523+0113	0.2376	17.3	204 ± 11	184 ± 18	189 ± 19	11.29 ± 0.03	0.78 ± 0.03	3.03 ± 0.11

Table 2. The 'correction factors' used to treat the line-index strengths of the UCMGs, such that they can be directly compared to SSP models with resolution 60 km s^{-1}[C(60 km s^{-1}= 1)]. See Section 3.3.1 for more details.

Correction factor	Mg$_b$	Fe5270	Fe5335	⟨Fe⟩
C(200 km s^{-1})	1.043	1.138	1.202	1.168
C(250 km s^{-1})	1.090	1.207	1.339	1.269
C(300 km s^{-1})	1.152	1.281	1.511	1.385
C(400 km s^{-1})	1.306	1.439	1.959	1.655
C(550 km s^{-1})	1.596	1.740	2.850	2.153

or more indices being contaminated by the sky or bad pixel lines. We therefore attach a 'flag' to all the systems that lie outside the grid and assign an uncertainty of 0.4 (the maximum possible) to the [Mg/Fe] values of these systems.

3.3.2 Mass-weighted stellar ages and metallicities from full-spectral fitting

Mass-weighted stellar ages and metallicities[13] are obtained using PPXF, which performs a full-spectral fit on the log-rebinned and rest-framed 1D SDSS spectra to which a multiplicative polynomial of degree 8 is applied to correct the shape of the continuum.[14] For the stellar population fit, the wavelength range is restricted to [3600–6500]Å since it is the cleanest spectral region (as discussed in Section 3.1) and the one where varying the low-mass end of the IMF would give a minimal contribution. Additionally, we only use models with ages up to the age of the Universe at the redshift of each galaxy, since it would not make physical sense to use models corresponding to older ages. Finally, we limit ourselves to models in the 'safe

[13]Light-weighted quantities are provided in the master catalogue.
[14]In appendix A of the INSPIRE Pilot we performed a test to assess how the stellar population results change when varying the degree of the polynomial. We refer the reader to that paper for a more detailed information.

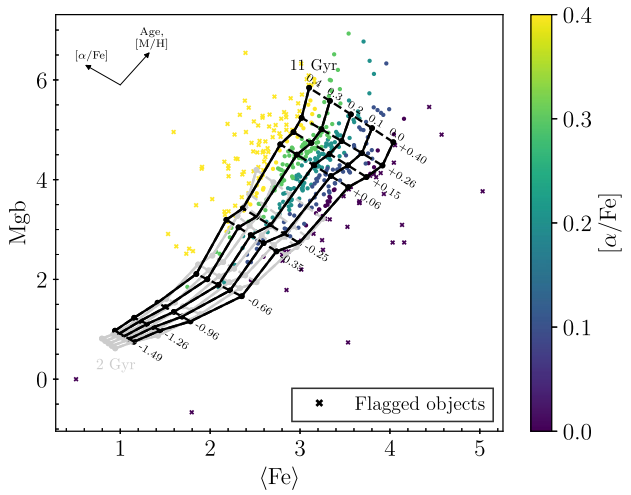

Figure 6. Mg_b–⟨Fe⟩ index–index plot. The grid shows MILES SSPs with two different ages (2 Gyr in grey and 11 Gyr in black), covering a range of metallicities from −1.49 to +0.40 (solid lines) and a range of [α/Fe] values between 0.0 and 0.4 (dashed lines). These models have a resolution of 60 km s^{-1}. The UCMGs are colour-coded by their derived value of [α/Fe]. The direction of variation for age, [M/H], and [α/Fe] is given by arrows in the top-left corner. Galaxies falling outside the model grid are highlighted with crosses and flagged in the catalogue.

range', i.e. metallicities up to [M/H] = 0.26 dex. This is different from what we did in previous INSPIRE papers but it is the most conservative choice. In fact, models with higher metallicities are not considered 'safe' for full-spectral fitting due to the lack of stars in the solar neighbourhood with metallicity higher than [M/H] $\sim$ 0.2 dex, upon which the MILES models are based (Vazdekis et al. 2012, 2015). Nevertheless, we note that the addition of the model with [M/H] = 0.4 dex does not heavily affect the age estimates and hence the reconstructed SFHs. We discuss how this influences our results in Appendix A.

Similarly to INSPIRE DR3, for each UCMG, we perform four different PPXF runs as described below. In all cases, we work in the 2D space where only age and metallicity are free to vary during the fits. Furthermore, in all the PPXF fits, we also fit gas lines (purple lines in Fig. 7), using the standard list given by PPXF as these might influence the age and metallicity estimates, especially when the emissions are superimposed on stellar absorptions. However, due to the large number of UCMGs, we cannot proceed in the same way as previous INSPIRE papers where we used the regularization method, repeating the fit multiple times for each galaxy until finding the maximum regularizing factor allowed by the data (see INSPIRE DR1 and INSPIRE DR3 for more information). Hence, we use a slightly different approach, as described below. First, we perform a lightly regularized fit with a regularization of 10 for all systems, using models with [α/Fe] equal to the [Mg/Fe] SSP-equivalent values found from the index–index analysis (see Section 3.3.1). Then, since the inferred [α/Fe] have an uncertainty of 0.1, we run PPXF again, once with [α/Fe] = [Mg/Fe] + 0.1 and once with [α/Fe] = [Mg/Fe] − 0.1. For 'flagged objects', we instead perform these fits using models with [α/Fe] = 0.0 and [α/Fe] = 0.4, hence deriving the most extreme SFHs for these objects.

At this point, we perform an unregularized fit with the 'true' [α/Fe] and use a bootstrapping method ('wild bootstrapping', described in Davidson & Flachaire 2008) to obtain a distribution of the weights assigned to each SSP template. This is similar to, although much quicker than, the regularization process which smooths the stellar population solution as much as the data allows. The main difference is that when performing regularized fits, one must manually (or iteratively) try different regularization values, each time rescaling the noise level, until reaching the MAX_REGUL for which the χ^2 increases by $\sqrt{2 \times N_{\rm pixel}}$ (where $N_{\rm pixel}$ is the number of pixel used in the fit). The MAX_REGUL changes system by system, which would have make this procedure very time consuming with $\sim$400 galaxies. We follow the procedure recommended by the author of PPXF where we use bootstrapping of the residuals, while repeating the PPXF fits 9 times to obtain averages for the stellar ages and metallicities (Cappellari 2017, 2023). Note that we run the fits where [α/Fe] is varied from the 'true' value without bootstrapping. We also tested different numbers of iterations for the bootstrapping routine (up to 20), finding negligible differences on the distribution of the weights. We also test that the results obtained with the bootstrapping procedure are compatible with the ones obtained with the regularization, on ten randomly selected spectra.

We finally calculate mean values and standard deviations for the mass-weighted stellar ages and metallicities from all the fits performed for each system (the three non-bootstrapped runs with varying values of [α/Fe] and the bootstrapped run). These are listed, along with the [Mg/Fe] ratios derived in Section 3.3.1, for a selection of UCMGs in Table 3. The same quantities for the entire sample are available in the catalogue released online as part of this publication. Fig. 7 shows two examples of (non-bootstrapped) PPXF fits for objects with very different SFHs. The galaxy spectra are plotted on the left and the weights of the age and metallicities are plotted on the right. The upper galaxy is much older and had all of its stellar mass formed in one burst (i.e. it is a relic). On the other hand, the galaxy on the bottom panel is much younger and has a much more extended SFH.

4 RESULTS

In this section, we use the stellar population parameters computed from the analysis described in Section 3 to reconstruct the SFHs of the UCMGs, as well as their stellar metallicity evolutions in cosmic time. This allows us to divide them into different groupings, computing their DoR and investigating how it relates to their stellar population properties. We will discuss how the assumptions we made influence the DoR in the dedicated Appendix A.

4.1 Time evolution of mass and metallicity

From the weights of the SSP models PPXF uses in the fit, we can infer the cosmic evolution of the stellar mass (i.e. the fraction of stellar mass assembled from the big bang to the present day) and of the stellar metallicity.

To calculate the cumulative stellar mass assembled in cosmic time (i.e. the SFH), we follow the receipt from previous INSPIRE papers. We start from the density maps, like the ones shown in the right panels of Fig. 7. We flip the age axis and sum over all metallicity values, computing in this way the fraction of mass assembled at each age bin since the big bang to the redshift of the galaxy.

To calculate the metallicity of a galaxy as a function of cosmic time (the metallicity evolution history or MEH), we follow instead Bevacqua et al. 2024 (specifically equation 5). For each cosmic time, we calculate the corresponding metallicity by computing the weighted mean of the metallicities of the subset of SSP models whose ages are older than that cosmic time. To build up the MEH curves, at the earliest cosmic time, we only consider the models with the oldest ages, whereas for 'today', i.e. at the redshift of the galaxy,

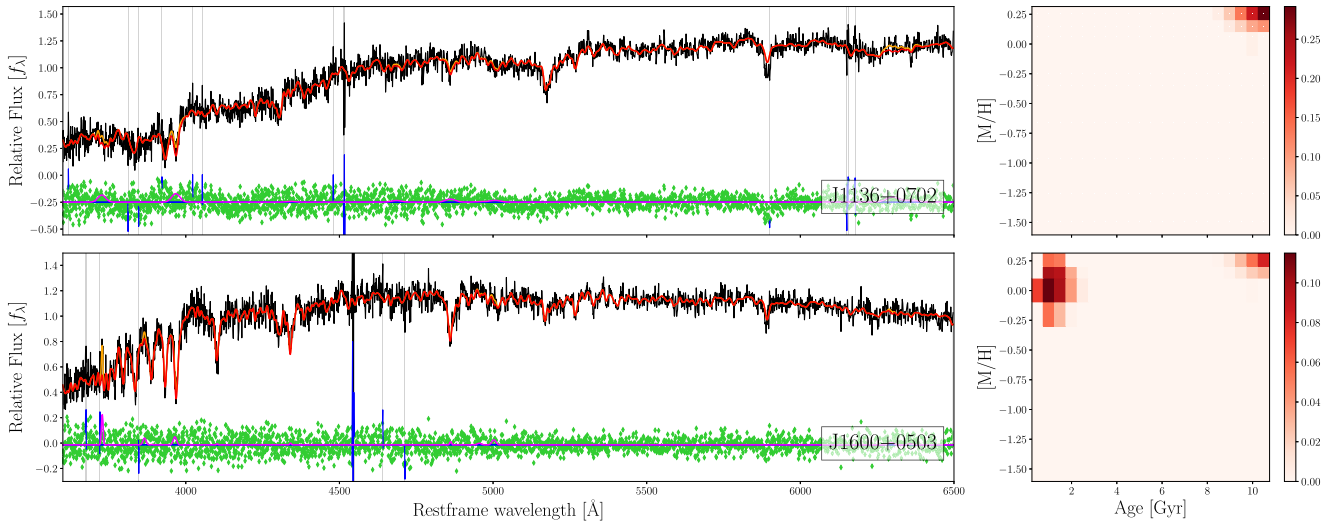

Figure 7. PPXF fits for two galaxies with very different SFHs. Left panel: the fits with the galaxy spectra in black, the SSP best-fitting template in red, residuals in green, pixels masked out from the fit in blue, and gas lines and fit in orange and purple, respectively. Right panel: the mass-weighted age–metallicity density maps for the non-bootstrapped (and lightly regularized) fits.

we consider all the models so that the metallicity matches with the metallicity computed in Section 3.3.2.

We note that this method of computing the cumulative mass and the metallicity at a given cosmic time assumes that stars form in a series of bursts rather than over an extended period of time (i.e. we use SSPs rather than models with time-declining star formation).

A selection of SFHs (top) and MEHs (bottom) are shown in Fig. 8 for objects that are representative of the entire sample. For each galaxy, whose ID is given in the title, the black line shows the mean quantity (stellar mass or metallicity) at each cosmic time and the shaded region represents one standard deviation around it. Vertical grey lines show the end of the first phase of the formation scenario ($z \sim 2$, Zolotov et al. 2015) and the age of the Universe at the redshift of the system (today). In the top panels, the horizontal lines highlight the 25 per cent and 75 per cent thresholds on the stellar mass to guide the eyes. From left to right, the objects vary from UCMGs with very peaked and quick SFHs that occurred very early on in cosmic time (i.e. extreme relics), to UCMGs with much more extended SFHs that completed their stellar mass assembly only very recently.

We note that the SSPs' binning is 0.5 Gyr and that we use, for each galaxy, only models with ages up to the age of the Universe at the redshift of the systems. We therefore cannot deduce anything about the SFH or the MEH of the galaxies for the cosmic time between the big bang and the formation of the oldest SSP models and so this period is masked out in Fig. 8. The exact region which is masked out varies depending on the age of the Universe at the redshift of the galaxy.

The MEHs show a wide range of behaviours, even for objects with similar SFHs. This is particularly true for UCMGs with more extended SFHs (the two right-most columns in Fig. 8), where we observe varying behaviours, resulting in objects spanning a wide range of metallicities across cosmic time. There are also cases where the metallicity stays roughly constant despite the mass increasing and vice versa, where the metallicity changes drastically despite the mass staying roughly constant. In contrast, relics and especially the most extreme ones, tend to have metallicities that stay fairly constant and super-solar at all cosmic times. As we will discuss later, this reflects the fact that relics are generally metal richer than younger UCMGs. Spatially resolved data will be necessary to further investigate the metallicity, its relation with SFHs, and its evolution with cosmic time.

4.2 DoR and relic confirmation

Following the same approach as in INSPIRE DR3, we compute for each UCMG the DoR as follows:

$$\mathrm{DoR} = \left[f_{\mathrm{M}^\star_{t\mathrm{BB}=3}} + \frac{0.5\ \mathrm{Gyr}}{t_{75}} + \frac{0.7\ \mathrm{Gyr} + (t_{\mathrm{Uni}} - t_{\mathrm{fin}})}{t_{\mathrm{Uni}}} \right] \times \frac{1}{3}, \qquad (2)$$

where $f_{\mathrm{M}^\star_{t\mathrm{BB}=3}}$ is the fraction of stellar mass at $z \sim 2$, t_{75} is the cosmic time at which 75 per cent of the stellar mass was in place, t_{fin} is the final assembly time (100 per cent of the stellar mass in place), and t_{Uni} is the age of the Universe at the redshift of the objects. The values 0.5 and 0.7 Gyr are chosen such that the DoR ranges between 0 and 1 (as explained in INSPIRE DR3). A higher DoR indicates an object with a very peaked SFH that formed most of its stellar mass by $z \sim 2$ (i.e. a relic), whereas a lower DoR indicates an object with a much more extended SFH with star formation continuing until recently (or still ongoing). We caution the reader that the DoR is an arbitrarily computed, dimensionless number which is useful to weigh the fraction of very old, 'pristine' stars and hence identify the most extreme relics, but that depends on the choices and assumptions made during the fit, as shown in Appendix A.

We first determine estimates of the parameters $f_{\mathrm{M}^\star_{t\mathrm{BB}=3}}$, t_{75}, and t_{fin} for the four PPXF fits performed for each object (as described in Section 3.3.2). We then choose the estimates which give the most conservative (lowest) estimate of the DoR, i.e. we use the minimum value of $f_{\mathrm{M}^\star_{t\mathrm{BB}=3}}$ and the maximum values of t_{75} and t_{fin},[15] to reproduce exactly what was done in previous papers. We however caution the readers that these are arbitrary choices that have an influence on the final DoR distribution, as we highlight in Appendix A. Nevertheless

[15]The t_{fin} is defined as the cosmic time at which 99.8 per cent of the stellar mass is formed. This (conservative) choice is motivated by the findings of Salvador-Rusiñol et al. (2022) who found that even in the most extreme local relic, NGC1277, a sub-percentage of younger stars are found.

Table 3. Stellar population results for a representative selection of systems. For each system, we also report the SSP-equivalent [Mg/Fe]. We estimate the stellar age and metallicity by taking the mean of all the fits for each system (see Section 3.3.2). Note that J1510+0546 is both amongst the oldest and most metal rich systems, and so is only included once on the table for conciseness.

ID SDSS	[Mg/Fe] (dex)	$t_{\rm mean}$ (Gyr)	$[{\rm M/H}]_{\rm mean}$ (dex)
	Highest stellar ages		
J1616+2809	0.1	12.4 ± 0.1	0.224 ± 0.013
J1358+1327	0.3	12.4 ± 0.2	0.235 ± 0.004
J0750+2259	0.1	12.3 ± 0.3	0.235 ± 0.007
J1433+5315	0.2	12.2 ± 0.4	0.235 ± 0.001
J1426+1647	0.2	12.2 ± 0.3	0.236 ± 0.002
J1510+0546	0.3	12.1 ± 0.1	0.240 ± 0.004
	Median stellar ages		
J2146−0821	0.2	10.4 ± 0.5	0.209 ± 0.016
J0824+1038	0.3	10.4 ± 0.6	0.173 ± 0.014
J1107+6506	0.1	10.4 ± 0.5	0.216 ± 0.010
J1427+2107	0.4	10.4 ± 1.1	0.162 ± 0.034
J1520+2035	0.2	10.4 ± 0.4	0.210 ± 0.011
J1338+0541	0.3	10.4 ± 0.1	$0.224 \pm .004$
	Lowest stellar ages		
J1126+0612	0.0	3.5 ± 2.0	0.114 ± 0.078
J0905+3657	0.1	3.3 ± 0.8	0.141 ± 0.034
J2305−1033	0.1	3.2 ± 1.2	0.145 ± 0.050
J1602+0245	0.2	3.1 ± 2.1	0.115 ± 0.071
J1452+0253	0.0	2.9 ± 2.4	0.145 ± 0.088
J1600+0503	0.0	2.3 ± 1.5	0.061 ± 0.046
	Highest metallicities		
J1620+1722	0.2	11.6 ± 0.1	0.240 ± 0.007
J1710+3941	0.2	11.8 ± 0.4	0.240 ± 0.002
J2130+0307	0.2	12.1 ± 0.1	0.240 ± 0.003
J1508+6049	0.3	12.0 ± 0.2	0.240 ± 0.007
J1732+3102	0.3	11.5 ± 0.2	0.239 ± 0.002
	Median metallicities		
J1122+2017	0.2	10.4 ± 0.6	0.204 ± 0.011
J0752+3514	0.1	9.0 ± 1.6	0.203 ± 0.010
J0736+4336	0.0	9.8 ± 0.6	0.203 ± 0.016
J1540+3454	0.4	9.9 ± 0.2	0.203 ± 0.015
J1206+6207	0.1	7.2 ± 1.6	0.202 ± 0.026
J1505+3007	0.2	8.5 ± 2.5	0.202 ± 0.033
	Lowest metallicities		
J1227−0304	0.3	9.0 ± 1.2	-0.058 ± 0.188
J1511+3020	0.4	5.4 ± 1.7	-0.100 ± 0.074
J0901+2242	0.0	9.1 ± 0.5	-0.125 ± 0.164
J2223-0012	0.3	6.2 ± 2.1	-0.211 ± 0.141
J1357+1553	0.2	6.7 ± 1.0	-0.231 ± 0.238
J0815+0635	0.0	5.4 ± 1.3	-0.320 ± 0.129

we stress that, although the numerical values and normalization of the DoR is dependent on the assumptions, this quantity in all cases is able to describe the variety of SFHs that, in turn, corresponds to a wide range of systems, from the most extreme relics to relatively younger UCMGs that undergone a more complex and time-extended formation history.

The distribution of the resulting DoRs for the 430 UCMGs is shown in Fig. 9 (blue), where we also compare it with that of the INSPIRE galaxies (red). We note that there are a number of differences between the approach we follow here and that followed in previous INSPIRE publications. First, we use a different selection criterion to identify UCMGs which is based on density, rather than cuts at fixed stellar mass and radius. We do however limit ourselves to objects that can be considered as UCMGs according to the INSPIRE definition, by correcting the SDSS sizes to KiDS resolution and excluding objects with $R_{\rm e\,KiDS} > 2$ kpc and by excluding objects with $M_\star < 6 \times 10^{10}\,{\rm M}_\odot$. Furthermore, here we decided to exclude the metal-richest SSPs while we included them in previous papers. We investigate the effect of this difference in Appendix A (Figs A5 and A6).

We observe a peak in the distribution at DoR ~ 0.5, which is slightly higher than in INSPIRE DR3 where the peak is at DoR ~ 0.4. However, both distributions cover a similar range of DoR values: $0.05 <$ DoR < 0.9, reflecting the great variety of SFHs covered by both samples.

Fig. 10 shows the DoR plotted against $f_{{\rm M}^\star_{t_{\rm BB}=3}}$ (top), t_{75} (middle), and $(t_{\rm Uni} - t_{\rm fin})/t_{\rm Uni}$ (bottom) for both the objects in this paper and those in INSPIRE DR3. We remind the readers that the latter quantity is used to take into account the fact that the systems cover a range of redshifts ($0.01 < z < 0.3$). Hence renormalizing by the age of the Universe at each redshift allows us to directly compare the final assembly times of the different objects. However, this is also the quantity with the largest uncertainty, which is due to the fact that we set a very restrictive threshold (>99.8 per cent of the stellar mass in place). We investigate the impact of a slightly different choice for $t_{\rm fin}$ in Appendix A. Errors on the plotted quantities are determined by taking the standard deviation of the four estimates of each parameter. The 430 UCMGs found in this paper follow a very similar distribution to the objects in INSPIRE DR3.

In previous INSPIRE papers, we define relics as objects that had formed 75 per cent or more than their stellar masses by $z = 2$. Using this operative and '*ad hoc*' threshold, the lowest DoR at which we found a relic was 0.34. Following the same approach, hence considering only objects that formed 75 or more per cent of their mass during the first phase of the formation scenario, we would retrieve 359/414 UMCGs and, quite nicely, the lowest DoR would be fully consistent with the previous one (0.346). However, thanks to the much larger number statistics, we can now better distinguish the different behaviours for different DoR ranges, hence moving away from an arbitrary mass threshold. We distinguish three different regions, as indicated by the vertical dashed lines in Fig. 10. In particular we observe that

(i) DoR $\lesssim 0.3$. In this range, $f_{{\rm M}^\star_{t_{\rm BB}=3}}$ linearly increases with the DoR but is always <75 per cent, $t_{75} \sim 8$ Gyr (i.e. a constant) with a large scatter, and $t_{\rm fin} \sim t_{\rm Uni}$. These UCMGs had very extended SFHs and cannot be considered relics of the ancient Universe. We find 56 of these objects.

(ii) $0.3 \lesssim$ DoR $\lesssim 0.6$. In this case, $f_{{\rm M}^\star_{t_{\rm BB}=3}}$ keeps increasing with the DoR, although at a slower rate. In many cases, it reaches ∼100 per cent around DoR∼ 0.5, where a bending in $f_{{\rm M}^\star_{t_{\rm BB}=3}}$ is visible. $t_{\rm fin}$ is still $\sim t_{\rm Uni}$, but now t_{75} starts to decrease with the DoR and the overall scatter is much smaller. These objects, although having formed the great majority of their stellar mass early on in cosmic time, still have a non-negligible fraction of stars that formed later on and/or through time-extended processes. There are 293 of these objects in our catalogue.

(iii) DoR $\gtrsim 0.6$. For these objects, $f_{{\rm M}^\star_{t_{\rm BB}=3}} \sim 100$ per cent, $t_{75} \sim 1$ Gyr, and $(t_{\rm Uni} - t_{\rm fin})/t_{\rm Uni}$ increases linearly with the DoR. Furthermore, above this threshold, the scatter in all three quantities becomes very small and the entire totality of the stellar mass budget is dominated by stars almost as old as the Universe. We find 81 of these extreme relics.

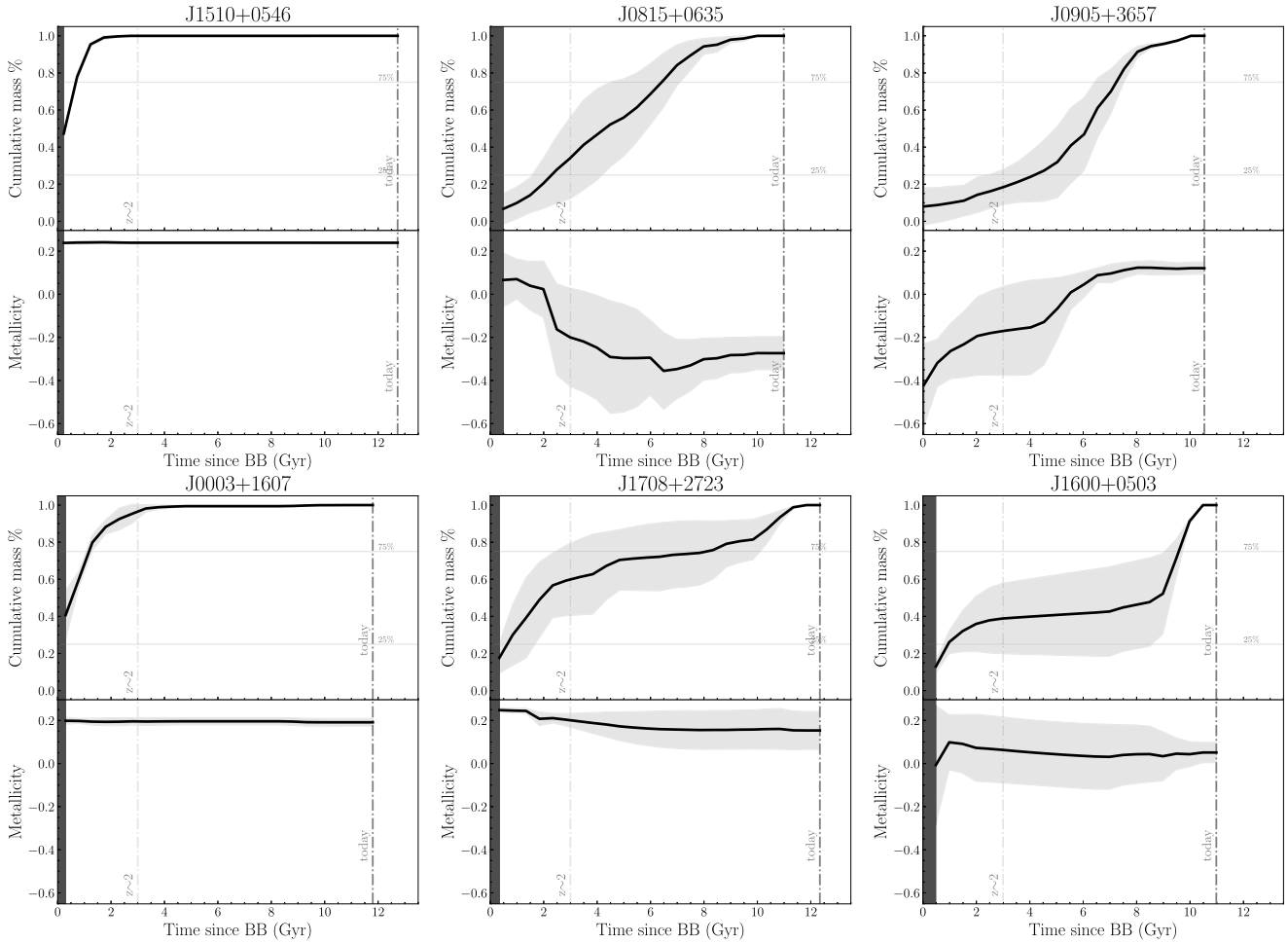

Figure 8. Stellar mass assembly and metallicity evolution in cosmic time, from the BB to the redshift of the galaxy, for a selection of six galaxies. In the top panel of each row, the black line shows the mean stellar mass at each cosmic time of the four fits (as described in Section 3.3.2). In the bottom panel of each row, the black line show the mean metallicity at each cosmic time of the four fits (also as described in Section 3.3.2). In both rows, the shaded region is one standard deviation around the mean for each cosmic time. The ID of each galaxy is reported above each galaxy.

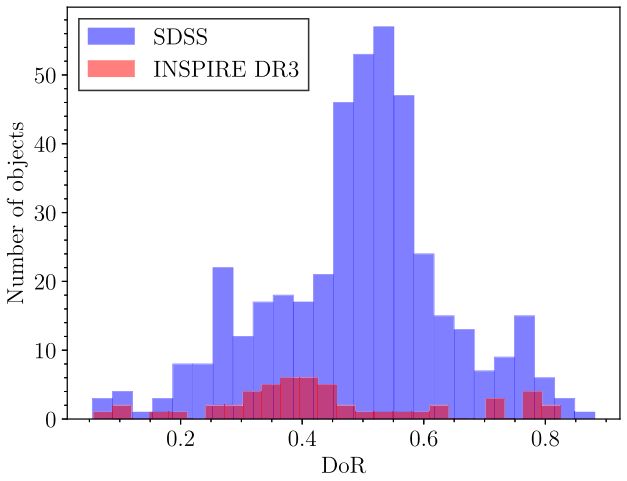

Figure 9. A comparison of the distribution of DoR values for the objects in this paper and the objects found previously in INSPIRE DR3.

We note that the second threshold was slightly higher with the original sample of 52 UCMGs (extreme relics were defined to have DoR$\geq$ 0.7). Now, having increased the sample by almost a factor of 10, we reconsider the groupings based on the new distributions.

Grèbol-Tomàs, Ferré-Mateu & Domínguez-Sánchez (2023) analysed a sample of 37 compact galaxies with MaNGA (Bundy et al. 2015) data, selected to bridge the stellar mass gap between compact elliptical galaxies ($8 \leq \log[M_\star/\mathrm{M}_\odot] \leq 10$) and UCMGs ($10 \leq \log[M_\star/\mathrm{M}_\odot]$). Using a machine learning based clustering algorithm (k-means), they classified the compact galaxies into three groups, according to their stellar properties. In particular, they used the cosmic time at which 90 and 50 per cent of the stars were formed, the stellar mass, metallicity and $\Sigma_{1.5}$ value for the classification. Interestingly, the classification we obtained is incredibly similar to the one they derived. They found that 76 per cent of their sample was made of old and metal rich galaxies with extremely steep SFHs. The remainder of the sample is almost equally split between intermediate-age galaxies with a wide range of metallicites (13 per cent) and young galaxies, showing multiple episodes of star formations (11 per cent). Both these groups are characterized by slightly α-enhanced stars, with lower [α/Fe] ratios than the first group.

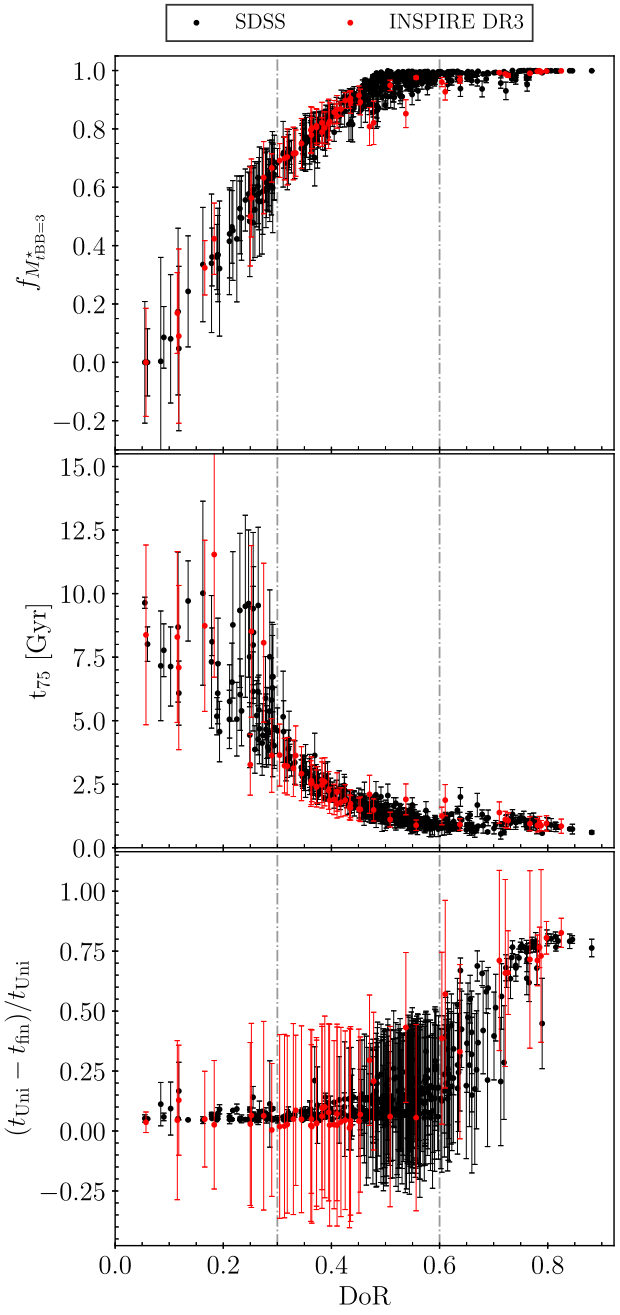

Figure 10. The DoR plotted against the fraction of stellar mass formed by $z \sim 2$ (top), the cosmic time at which 75 per cent of the stellar mass was in place (middle), and the time of final assembly (bottom). We compare these values computed for objects in SDSS (black) with those computed for objects in INSPIRE DR3 (red). We also draw vertical lines at DoR = 0.3 and DoR = 0.6 to indicate changes in behaviour of each quantity, as described in Section 4.2.

In Fig. 11, we show the relation between the DoR and a selection of other quantities. Although with a large scatter, we confirm the previous findings that UCMGs with higher DoR are generally metal richer, are older (by construction), and have lower sSFRs. We also find that there is a negligible correlation between DoR and R_e. Furthermore, a weak indication that they also have larger stellar velocity dispersions is hinted at in the plot. This is however only evident for DoR > 0.6, which is fully consistent with what we found in INSPIRE DR3 (specifically in Fig. 9). Interestingly, around the same value of DoR > 0.6, the scatter in [M/H] sharply decreases and all the UCMGs are consistent with a super-solar metallicity, reaching the maximum value allowed by the MILES models ([M/H] = 0.26 dex). The distribution of [α/Fe] for the UCMGs is shown in Fig. 12, where we split the objects into the three groupings based on DoR described earlier in this section.[16] We find that, in general, objects belonging to the group with the lowest DoRs have lower [α/Fe] values than the other two groups. Additionally, objects with the highest DoR values (DoR > 0.6) have the highest [α/Fe] values on average, confirming previous findings that UCMGs with higher DoR have slightly higher [α/Fe] ratios. This suggests that a high [Mg/Fe] value (from which [α/Fe] is inferred) is an additional good criterion from which to search for relics.

Since the relation between DoR and metallicity is tighter than that between DoR and $\sigma_\star$ or DoR and [α/Fe], we suggest that an even better way to select relics from a large sample of spectroscopically confirmed UCMGs is to select metal-rich objects. To further illustrate this, in Fig. 13, we divide the UCMGs into three groups (based on the subdivisions described earlier) and then further divide each group into bins of different mass. For each subdivision, we compute the mean and standard deviation of the stellar mass, metallicity (top panel), and velocity dispersion (bottom panel) and plot these points. It is very clear that objects at the top of these distributions tend to have higher DoRs, especially for the metallicity against stellar mass distribution. In this case, the most extreme relics at all mass bins saturate at the maximum metallicity value allowed by the SSP models in their 'safe' ranges.

5 CONCLUSIONS

This paper is the first of the E-INSPIRE project, which expands on the original INSPIRE sample with the goal of understanding relics, their formation, time evolutions and environment. In this first paper, we have pushed the redshift boundaries towards the local Universe and extended the original sample of UCMGs with a measured DoR (Spiniello et al. 2024) by a factor of $\sim$10, hence bridging the gap with the local Universe. This has been made possible by the much larger sky area covered by the SDSS survey, with respect to KiDS. We started by selecting galaxies from SDSS DR18 (Almeida et al. 2023) at $z < 0.4$ with red colours and high stellar velocity dispersion ($\sigma_\star > 200\,{\rm km\,s^{-1}}$). Furthermore, we used stellar mass estimates from the GSWLC-2 catalogue described in Salim et al. (2018) and estimated the effective radii by combining de Vaucouleurs and exponential radii, directly provided by SDSS. Since the GSWLC-2 only goes up to $z < 0.3$, we further reduce the upper redshift boundary of our final sample. We then selected the densest and most compact objects using the criterion of Baldry et al. (2021), first defined in Barro et al. (2013). We finally assembled a catalogue of 430 spectroscopically confirmed UCMGs, after further cleaning the sample by manually inspecting their stamps and spectra and correcting for the worse spatial resolution of SDSS compared to KiDS. To our knowledge, at the time of writing, this is the largest homogeneously selected catalogue of spectroscopically confirmed UCMGs at $0.01 < z < 0.3$. The catalogue is publicly available for the entire scientific community and includes coordinates, Petrosian

[16]The peaks in the distribution are artificially created by the [α/Fe] sampling of 0.1.

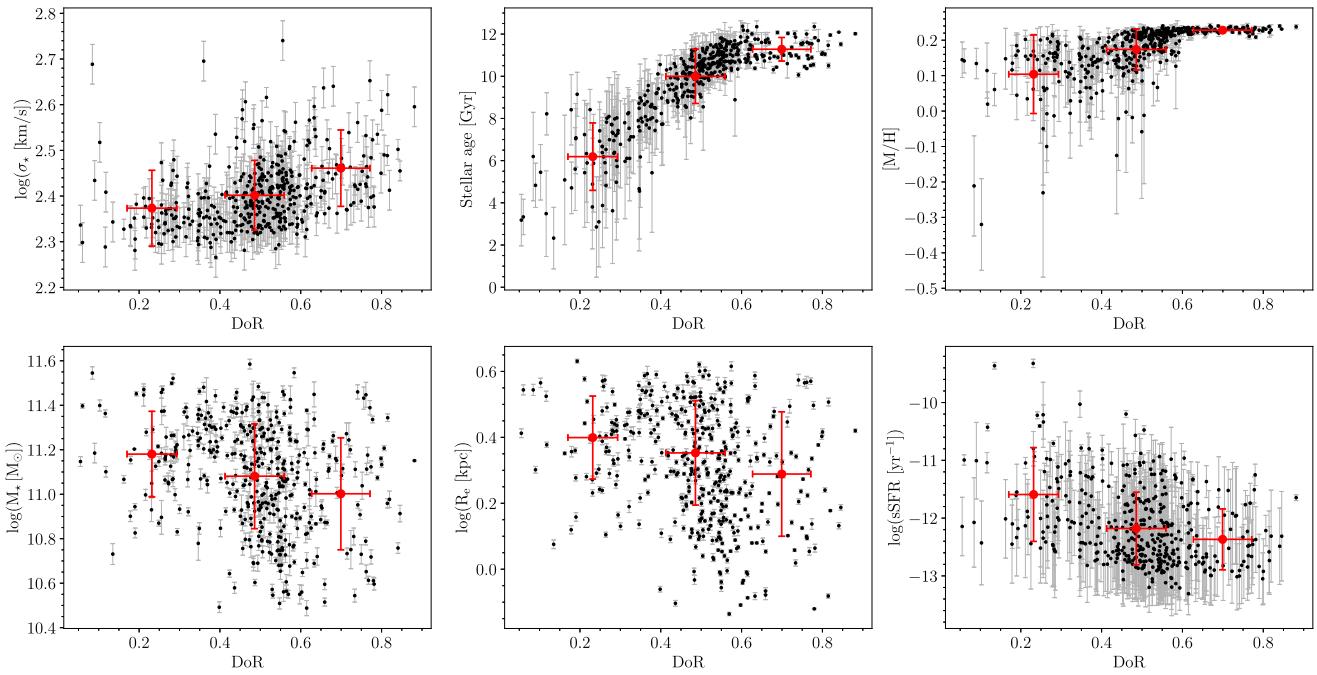

Figure 11. The relationship between the DoR and (from top left to bottom right) stellar velocity dispersion, age, metallicity, stellar mass, effective radii (as defined in Section 2.3), and specific SFRs. The objects have also been grouped by DoR, following the groupings outlined in Section 4.2. For each group, the mean and standard deviation have been plotted in the panels as red circles with errorbars.

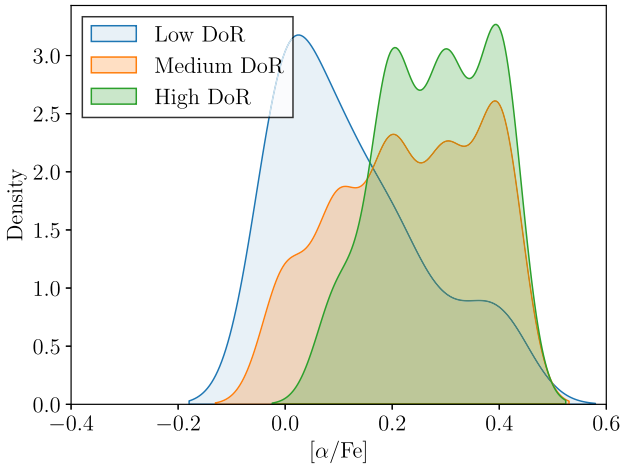

Figure 12. The distribution of [α/Fe] for the 430 UCMGS. These have been split into three groupings based on DoR, as described in Section 4.2. The 'Low DoR' groups contains objects with DoR $\lesssim 0.3$, the 'High DoR' group contains objects with DoR $\gtrsim 0.6$, and the 'Medium DoR' group contains everything in between ($0.3 \lesssim$ DoR $\lesssim 0.6$). This plot is produced by smoothing the distribution with a Gaussian kernel to improve visibility.

r-band magnitudes, stellar masses, sSFRs, and effective radii. These quantities are all computed from optical photometric data. In addition, we provide integrated stellar velocity dispersion values as well as stellar population parameters that we estimated from SDSS spectra, as described in Section 3. Finally, the DoR and the ingredients used to compute it, as well as the stellar population parameters, are listed in the catalogue for all the objects.

Through a spectroscopic stellar population analysis, based on both full spectral fitting and line-index analysis, we have found that:

(i) the UCMGs cover a wide range of DoR, from 0.05 to 0.88, tracing a wide variety in SFHs;

(ii) the metallicity profiles are generally constant in time for extreme relics, but can vary quite dramatically for objects with a medium or low DoR;

(iii) based on the dependence of the DoR on fraction of stellar mass assembled by $z \sim 2$, the time at which 75 per cent of the mass was in place, and the time of final assembly, we can divide the UCMGs into three DoR groups. Objects with DoR $\lesssim 0.3$ are characterized by $f_{M^{\star}_{rBB=3}} < 0.7$, a constant $t_{75} \sim 8$ Gyr, and a t_{fin} as large as the Universe age at the redshift of each object. At intermediate DoR more than 60 per cent of the mass was formed at early cosmic time and hence the objects can be considered as relics. For $0.3 \lesssim$ DoR $\lesssim 0.6$, $f_{M^{\star}_{rBB=3}}$ increases and t_{75} decreases with increasing DoR but t_{fin} is still $\sim t_{Uni}$. Finally, for DoR > 0.6, the totality of the stellar mass was assembled less than 3 Gyr from the big bang (hence $t_{fin} << t_{Uni}$). This indicates that by looking at the three quantities combined into the DoR, one can truly distinguish between the variety of SFHs found among the UCMGs;

(iv) UCMGs with DoR $\gtrsim 0.6$ are older by construction and are consistently metal richer, hitting the maximum value allowed by the SSP models with a very small scatter. They also have larger stellar velocity dispersion, smaller sSFRs, and larger [Mg/Fe] ratios. They are undoubtedly the most extreme relics of the Universe.

We confirmed 374 new ultra-compact objects at $0.01 < z < 0.3$ that have formed the majority ($\gtrsim$70 per cent) of their stellar mass during the first phase of the two-phase formation scenario. Of these, 81 were fully in place by $z \sim 2$ and assembled the entire totality of their stars soon ($\lesssim$3 Gyr) after the big bang. The main conclusion of this paper is thus that selecting compact objects with a combination of large velocity dispersion values ($\sigma_{\star} \geq 250\,\mathrm{km\,s^{-1}}$), super-solar metallicities ([M/H] ≥ 0.2), old ages, and high [Mg/Fe] ratios is the most efficient way to find relics.

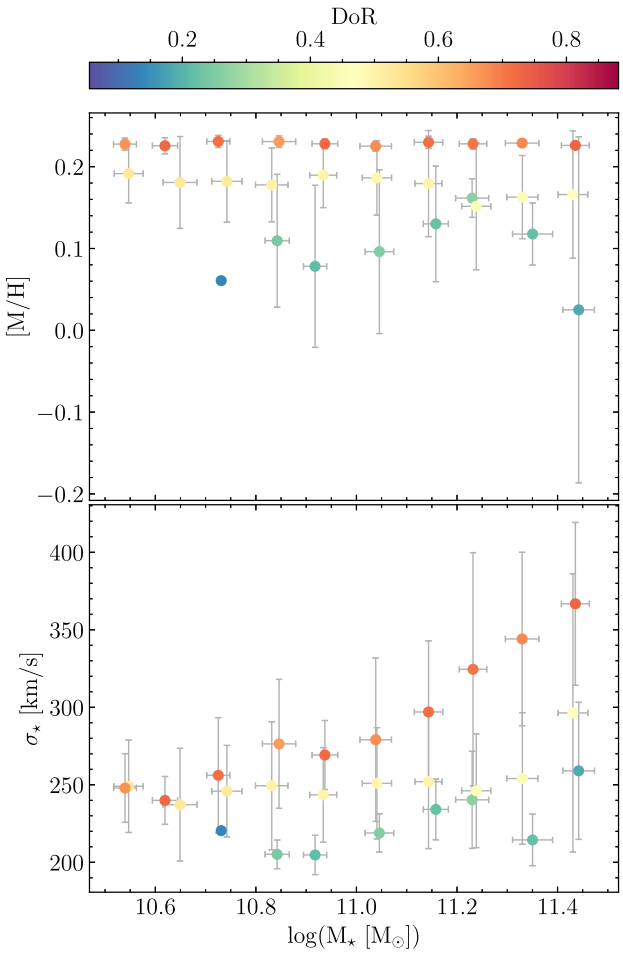

Figure 13. Plots of stellar mass against metallicity (top panel) and velocity dispersion (bottom panel). As described in Section 4.2, the UCMGs are divided into groups of similar DoR (based on the discussion in that section) and stellar mass. The mean and standard deviation of each group are then plotted on the above figure.

Having assembled a statistically large sample of UCMGs with a variety of DoR will allow us, in the future, to compare this population with normal-sized galaxies of similar stellar masses. Indeed, one of the future plans of E-INSPIRE will be to compute the DoR in the innermost region of larger ETGs at similar redshifts, and compare the results we obtained for UCMGs so far.

ACKNOWLEDGEMENTS

CS and CT acknowledge funding from the INAF PRIN-INAF 2020 programme 1.05.01.85.11. AFM has received support from RYC2021-031099-I and PID2021-123313NA-I00 of MICIN/AEI/10.13039/501100011033/FEDER,UE, NextGenerationEU/PRT. CT acknowledges the INAF grant 2022 LEMON. GD acknowledges support by UKRI-STFC grants: ST/T003081/1 and ST/X001857/1. JPVB received the support of a fellowship from the 'la Caixa' Foundation (ID 100010434). The fellowship code is LCF/BQ/DI23/11990084.

DATA AVAILABILITY

An online master catalogue presenting the stellar population results, as well as morphological and photometrical quantities for all 430 UCMGs is associated to this publication. This is publicly available for download from the E-INSPIRE website: https://sites.google.com/inaf.it/chiara-spiniello/e-inspire

REFERENCES

Abazajian K. et al., 2004, AJ, 128, 502
Almeida A. et al., 2023, ApJS, 267, 44
Astropy Collaboration, 2022, ApJ, 935, 167
Baldry I. K., Sullivan T., Rani R., Turner S., 2021, MNRAS, 500, 1557
Barbosa C. E., Spiniello C., Arnaboldi M., Coccato L., Hilker M., Richtler T., 2021, A&A, 649, A93
Barro G. et al., 2013, ApJ, 765, 104
Bevacqua D. et al., 2024, A&A, 690, A150
Blanton M. R. et al., 2001, AJ, 121, 2358
Bolton A. S. et al., 2012, AJ, 144, 144
Bundy K. et al., 2015, ApJ, 798, 7
Cappellari M., 2017, MNRAS, 466, 798
Cappellari M., 2023, MNRAS, 526, 3273
Cappellari M., Emsellem E., 2004, PASP, 116, 138
Cappellari M. et al., 2013, MNRAS, 432, 1709
Charbonnier A. et al., 2017, MNRAS, 469, 4523
Clerici K. S., Schnorr-Müller A., Trevisan M., Ricci T. V., 2024, MNRAS, 531, 1034
Costantin L. et al., 2019, A&A, 632, A9
D'Ago G. et al., 2023, A&A, 672, A17
Damjanov I., Abraham R. G., McCarthy P. J., Glazebrook K., 2009, American Astronomical Society Meeting Abstracts #213. p. 512
Davidson R., Flachaire E., 2008, J. Econometrics, 146, 162
Davies R. L., Sadler E. M., Peletier R. F., 1993, MNRAS, 262, 650
Ferré-Mateu A., Trujillo I., Martín-Navarro I., Vazdekis A., Mezcua M., Balcells M., Domínguez L., 2017, MNRAS, 467, 1929
Gallazzi A., Charlot S., Brinchmann J., White S. D. M., 2006, MNRAS, 370, 1106
Gallazzi A. R., Pasquali A., Zibetti S., Barbera F. L., 2021, MNRAS, 502, 4457
Grèbol-Tomàs P., Ferré-Mateu A., Domínguez-Sánchez H., 2023, MNRAS, 526, 4024
Huertas-Company M. et al., 2016, MNRAS, 462, 4495
Khramtsov V. et al., 2019, A&A, 632, A56
Kuijken K., 2011, The Messenger, 146, 8
Kuntschner H., 2004, A&A, 426, 737
La Barbera F., de Carvalho R. R., Kohl-Moreira J. L., Gal R. R., Soares-Santos M., Capaccioli M., Santos R., Sant'anna N., 2008, PASP, 120, 681
Liu Y., 2020, MNRAS, 497, 3011
Maksymowicz-Maciata M. et al., 2024, MNRAS, 531, 2864
Martín-Navarro I., Vazdekis A., Falcón-Barroso J., La Barbera F., Yıldırım A., van de Ven G., 2018, MNRAS, 475, 3700
Martín-Navarro I. et al., 2023, MNRAS, 521, 1408
Matteucci F., 1994, A&A, 288, 57
Naab T. et al., 2014, MNRAS, 444, 3357
Newman A. B., Ellis R. S., Bundy K., Treu T., 2012, ApJ, 746, 162
Oser L., Ostriker J. P., Naab T., Johansson P. H., Burkert A., 2010, ApJ, 725, 2312
Pernet E., Boecker A., Martín-Navarro I., 2024, A&A, 687, L14
Pietrinferni A., Cassisi S., Salaris M., Castelli F., 2004, ApJ, 612, 168
Pietrinferni A., Cassisi S., Salaris M., Castelli F., 2006, ApJ, 642, 797
Planck Collaboration VI, 2020, A&A, 641, A6
Riffel R., Borges Vale T., 2011, Ap&SS, 334, 351
Rousseeuw P. J., Van Driessen K., 2006, Data Mining and Knowledge Discovery, 12, 29
Salim S., Boquien M., Lee J. C., 2018, ApJ, 859, 11

Salvador-Rusiñol N., Ferré-Mateu A., Vazdekis A., Beasley M. A., 2022, MNRAS, 515, 4514
Saracco P. et al., 2020, ApJ, 905, 40
Saulder C., van den Bosch R. C. E., Mieske S., 2015, A&A, 578, A134
Scognamiglio D. et al., 2020, ApJ, 893, 4
Shen S., Mo H. J., White S. D. M., Blanton M. R., Kauffmann G., Voges W., Brinkmann J., Csabai I., 2003, MNRAS, 343, 978
Simard L., Mendel J. T., Patton D. R., Ellison S. L., McConnachie A. W., 2011, ApJS, 196, 11
Spiniello C., Trager S., Koopmans L. V. E., Conroy C., 2014, MNRAS, 438, 1483
Spiniello C. et al., 2021a, A&A, 646, A28
Spiniello C. et al., 2021b, A&A, 654, A136
Spiniello C. et al., 2024, MNRAS, 527, 8793
Stoughton C. et al., 2002, AJ, 123, 485
Thomas D., Maraston C., Bender R., Mendes de Oliveira C., 2005, ApJ, 621, 673
Tortora C. et al., 2016, MNRAS, 457, 2845
Tortora C. et al., 2018, MNRAS, 481, 4728
Trager S. C., Somerville R. S., 2009, MNRAS, 395, 608
Trujillo I., Cenarro A. J., de Lorenzo-Cáceres A., Vazdekis A., de la Rosa I. G., Cava A., 2009, ApJ, 692, L118
Trujillo I., Ferré-Mateu A., Balcells M., Vazdekis A., Sánchez-Blázquez P., 2014, ApJ, 780, L20
Vazdekis A., Ricciardelli E., Cenarro A. J., Rivero-González J. G., Díaz-García L. A., Falcón-Barroso J., 2012, MNRAS, 424, 3156
Vazdekis A. et al., 2015, MNRAS, 449, 1177
Vazdekis A., Koleva M., Ricciardelli E., Röck B., Falcón-Barroso J., 2016, MNRAS, 463, 3409
Vernet J. et al., 2011, A&A, 536, A105
Worthey G., 1994, ApJS, 95, 107
Worthey G., 1999, in Hubeny I., Heap S., Cornett R., eds, ASP Conf. Ser. Vol. 192, Spectrophotometric Dating of Stars and Galaxies. Astron. Soc. Pac., San Francisco, p. 283
Yasuda N. et al., 2001, AJ, 122, 1104
Yıldırım A., van den Bosch R. C. E., van de Ven G., Martín-Navarro I., Walsh J. L., Husemann B., Gültekin K., Gebhardt K., 2017, MNRAS, 468, 4216
Zolotov A. et al., 2015, MNRAS, 450, 2327

SUPPORTING INFORMATION

Supplementary data are available at *MNRAS* online.

suppl_data

Please note: Oxford University Press is not responsible for the content or functionality of any supporting materials supplied by the authors. Any queries (other than missing material) should be directed to the corresponding author for the article.

APPENDIX A: TESTING THE IMPACT OF THE FITTING ASSUMPTIONS ON THE DOR

For each UCMG in the catalogue that we have assembled in Section 2, we have derived SFHs and therefore the DoR. This dimensionless number is very useful in quantifying the fraction of very old stars formed during the first phase of the two-phase formation scenario (Oser et al. 2010; Naab et al. 2014; Huertas-Company et al. 2016). However, we have also stressed in the main body of the paper that this quantity strongly depends on the choices one makes for the full-spectral fitting. Therefore, in this appendix, we provide a more detailed and technical description of the impact of our assumptions on the DoR (normalization and distribution) and hence on the results presented in Section 4.

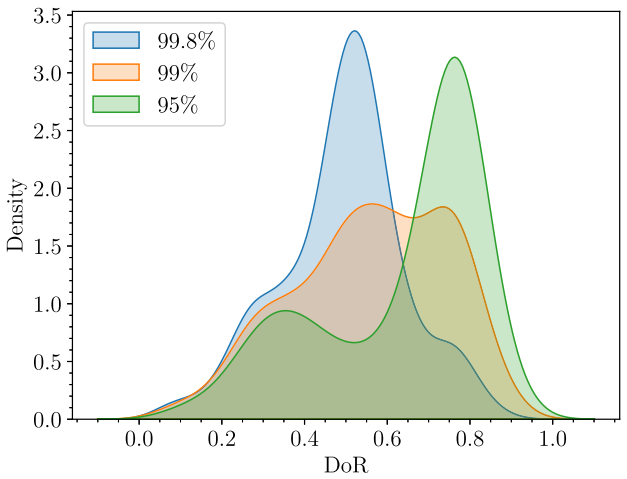

Figure A1. A comparison of how the DoR distributions changes for different choices of threshold when defining $t_{\rm fin}$. In blue, the distribution for when this threshold is 99.8 per cent of the stellar mass in place (as in this paper). In orange, the distribution for when this threshold is 99 per cent. In green, the distribution when this threshold is 95 per cent. This plot is produced by smoothing the distribution with a Gaussian kernel to improve visibility.

A1 Changing the threshold for the final assembly time

Among the different quantities used to compute the DoR, $t_{\rm fin}$ is that with the largest uncertainty (as noted in Section 4.2). We believe that this is because the spectral fit on the optical spectra is very sensitive to a sub-percentage fraction of very recent star formation. Especially when bootstrapping, it is likely that PPXF picks a few SSP models with very young ages, hence increasing the final time of assembly. This is especially evident when requiring a very conservative threshold of 99.8 per cent of the stellar mass being assembled, as we do in the main body of the paper. Hence, here we test the impact on the overall DoR distribution by lowering this threshold to 99 and to 95 per cent. Fig. A1 shows the current DoR, as obtained in the main text, in blue and the distributions with lower thresholds in orange and green respectively. As expected, reducing the threshold of stars being assembled pushes the distribution of DoRs towards the higher values. Interestingly, the 99 per cent threshold flattens the peak at ∼0.5, broadening the distribution across a larger range of DoR. Lowering the threshold to 95 per cent instead produces a peak at much higher DoR, with 291 objects classified as extreme relics (DoR > 0.6).

A2 Using mean or median quantities when computing DoR

In the computation of the DoR, we have used the most conservative estimates of the three single parameters: the minimum of $f_{M^{\star}_{tBB=3}}$, the maximum t_{75} and $t_{\rm fin}$. Clearly, this approach returns the minimum DoR for each object. Fig. A2 shows how the distribution would change if we used mean or median quantities instead. Predictably, using mean quantities shifts the overall distribution of DoRs towards much higher values. As a result, the number of extreme relics goes from 81 to 216 and the number of non-relics dramatically reduces from 56 to 16. The number of objects with $0.3 \lesssim$ DoR $\lesssim 0.6$ goes from 293 to 198. Using median quantities instead produces two different peaks, one identical to the original distribution derived with the most conservative parameters, and the other following the mean distribution. We also note that at very low DoR, the three distributions are similar.

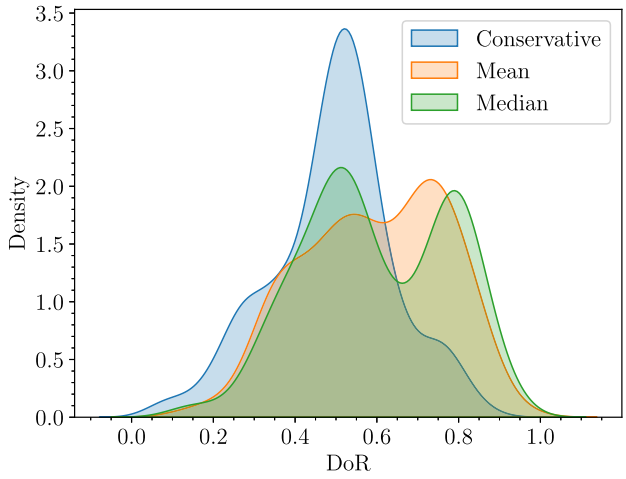

Figure A2. A comparison of the difference in DoR distributions when we use different estimates of $f_{M^{\star}_{iBB=3}}$, t_{75}, and t_{fin}. Here, we plot the distributions for the most conservative, mean, and median estimates of each quantity. This plot is produced by smoothing the distribution with a Gaussian kernel to improve visibility.

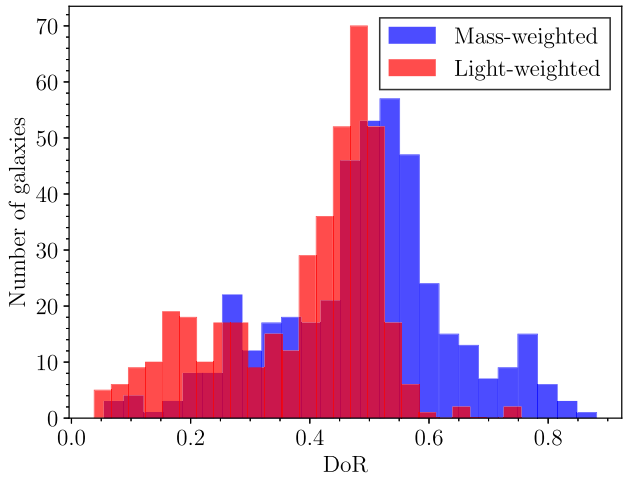

Figure A3. A comparison of the DoR distributions computed using mass-weighted population parameters versus light-weighted population parameters.

A3 Computing light-weighted ages and metallicities

Following previous INSPIRE publications, we have inferred mass-weighted ages and metallicities from the full-spectral fitting. This choice is motivated by the fact that mass-weighted quantities offer a direct probe of the integrated SFH and MEH. Since young stars outshine evolved ones, mass-weighted ages are always older than light-weighted ones. Furthermore, light-weighted ages and metallicities tend to artificially strengthen the observed trends with other parameters (e.g. velocity dispersion, Trager & Somerville 2009). In Fig. A3 we compare the DoR histograms obtained when computing mass-weighted ages (blue) and light-weighted ones (red). As expected, the overall effect is that the number of non-relics (DoR<0.3) is larger in the latter case.

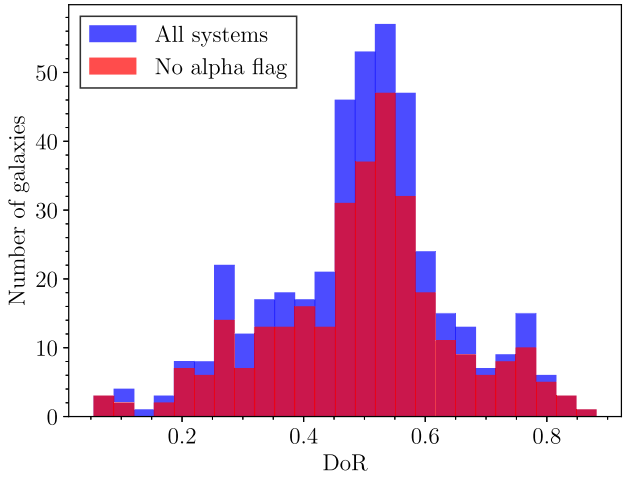

Figure A4. A comparison of the DoR distributions for the full set of UCMGs and excluding objects which were flagged (see Section 3.3.1).

A4 Removing flagged objects

In Section 3.3.1, we have used the Mg_b–⟨Fe⟩ index–index plot to infer the [Mg/Fe] abundances for the entire sample of 430 UCMGs. We have used the MILES SSP models to build a grid with [α/Fe] varying from 0 to 0.4 in steps of 0.1 on which we overplotted the systems. However, 116 objects fall outside the model grid and hence have been flagged. For these, we adopted the most conservative approach and ran PPXF using the two models with extreme [α/Fe] values (0.0 and 0.4). In the INSPIRE Pilot, we have shown that as [α/Fe] is increased, the ages generally become older and the SFHs become slightly more peaked. Hence, using the maximum range of [α/Fe] values to derive SFHs for the flagged objects produces the largest uncertainties and gives the most conservative result. Here, we confirm that this does not have an impact on the results we presented in the main paper. In fact, Fig. A4 shows that the distribution of the DoR when excluding the flagged objects is very similar to the one where they are included.

A5 Fitting with 'unsafe' SSP models

As noted in Section 3.3.2, we limit ourselves to SSP models in the 'safe ranges', i.e. those with metallicities up to [M/H] = 0.26 dex. This was strongly advised by the author of the models (private communication). However, our results suggest that relics tend to have super-solar metallicities, with a significant number reaching the highest metallicity allowed by the models. Here, we thus investigate the impact of including these 'unsafe' models. In Fig. A5, we plot the metallicities estimated without the [M/H] = 0.40 dex SSP models (main text) versus these estimated including them to show that this causes a shift towards higher metallicity for all systems in our sample, despite their DoR. Fig. A6 shows the DoR distribution shifts slightly towards lower values when [M/H] = 0.40 dex is included, suggesting that the effect of this change is to decrease the ages of these galaxies. This is unsurprising due to the age–metallicity degeneracy (Worthey 1994, 1999). We also note that the distribution including [M/H] = 0.40 dex is closer to that of the main paper compared to that of INSPIRE DR3, where indeed the 'unsafe' models were included in the PPXF fit.

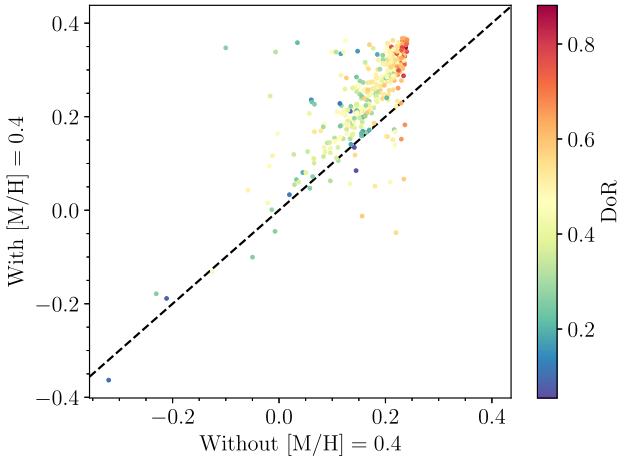

Figure A5. A comparison of how the computed metallicity changes when we include the [M/H] = 0.40 dex models. The dashed line indicates the 1-to-1 relation. The points are colour-coded by their DoR calculated without the [M/H] = 0.40 dex models.

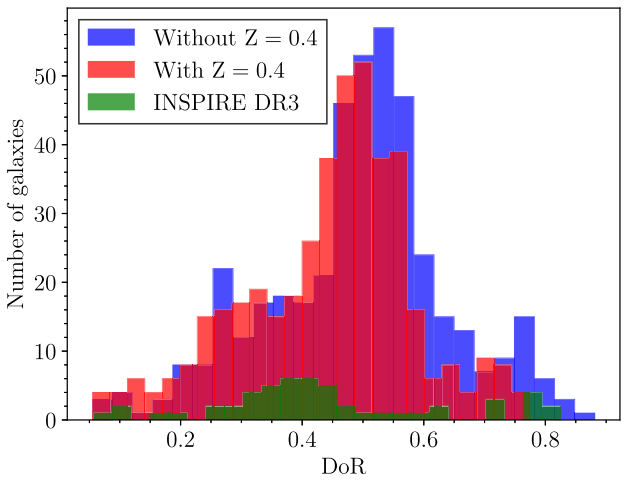

Figure A6. A comparison of the DoR distributions when limiting ourselves to SSP models in the 'safe ranges' (i.e. not including models with [M/H] = 0.40 dex) and when we use all available models (including [M/H] = 0.40 dex). The DoR distribution from INSPIRE DR3 (which uses [M/H] = 0.40 dex models) is included for comparison.

APPENDIX B: COMPARISON BETWEEN SIZE ESTIMATES FROM SDSS AND FROM KIDS

In this appendix, we compare the effective radii calculated in this paper (as described in Section 2.3) with the effective radii measured from KiDS data (Tortora et al. 2018; Scognamiglio et al. 2020). This is particularly crucial as estimating sizes of UCMGs from ground-based, seeing-limited imaging is very challenging. We point the readers to the appendix B of Tortora et al. (2018), which performs a detailed analysis on the expected systematics and statistical uncertainties on the effective radii estimates.

To compare the size estimates from SDSS and KiDS, we consider systems from the INSPIRE sample that are within SDSS DR18 (Almeida et al. 2023), of which there are 36 (out of 52). For these systems, we calculate their effective radii as measured by SDSS using

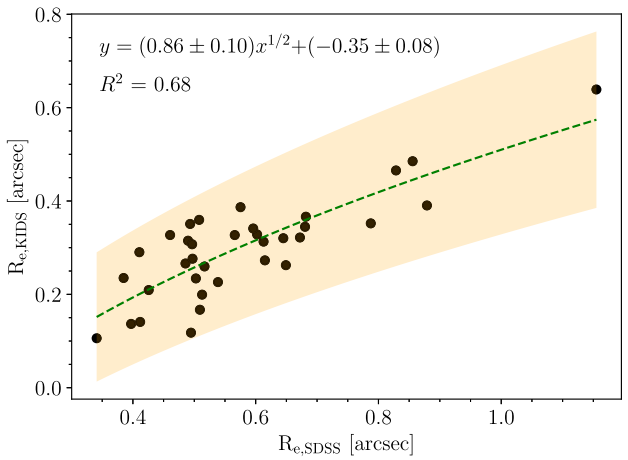

Figure B1. A comparison of the effective radii measured by SDSS and KiDS for a selection of systems in the INSPIRE sample. This is fitted with a quadratic (the dashed line), of which the equation (with errors) is shown. The R^2 value for this fit is also included.

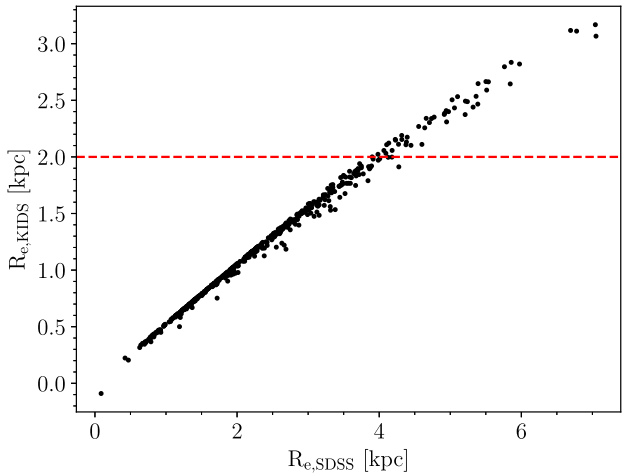

Figure B2. Sizes computed from SDSS imaging plotted against sizes corrected as they will be measured from KiDS higher resolution images.

the same procedure as Section 2.3. This measure of R_e is compared with that measured by KiDS in Fig. B1.

From this figure, we clearly see that the effective radii computed by SDSS are systematically larger than those inferred from KiDS. We speculate that this is caused by the worse spatial resolution (larger pixel size) and PSF FWHM of SDSS, which makes it harder to estimate precise effective radii, especially for these incredibly small objects.

We find that this scatter is fitted well by a non-linear equation with $R^2 = 0.68$ with $R_{e,KiDS}$ scaling as $\sqrt{R_{e,SDSS}}$. This indicates that the relation between the radii is quadratic in nature, which we suggest might be due to the PSF as the radial linear size goes with the 2D shape of the PSF, which relates to its area. Thus, we fit a quadratic relation to the points, deriving the following equation:

$$R_{e,KiDS} = (0.86 \pm 0.10)R_{e,SDSS}^{1/2} + (-0.35 \pm 0.08). \quad \text{(B1)}$$

We then use this equation to correct the sizes we derive for all the objects selected in Section 2.3, and hence to assemble the final sample of 430 ultra-compact galaxies. Fig. B2 shows the two estimates of

the effective radii one against each other. The horizontal dashed red line highlights the 2 kpc threshold that has been used, as in previous INSPIRE papers, to select 430 UCMGs. Given the worse resolution of SDSS imaging, this same threshold would correspond to sizes in SDSS of $\lesssim$4 kpc. Based on this correction, we finally select 446/495 objects (of which 430 are UCMGs, see main text for more details).

As already pointed out in INSPIRE DR3, the only way to precisely estimate structural parameters for UCMGs is to obtain AO supported or space observations.

This paper has been typeset from a TEX/LATEX file prepared by the author.